



A theory for ice-till interactions and sediment entrainment beneath glaciers

A. W. Rempel¹

Received 10 July 2007; revised 18 October 2007; accepted 14 November 2007; published 29 February 2008.

[1] The ice-till interface beneath soft-bedded glaciers can be marked by an abrupt transition from an ice layer above to unfrozen sediments below. Alternatively, the transition can be more gradual, with ice infiltrating the underlying sediments to form a fringe layer that contains a mixture of ice, liquid water, and sediment particles. The fringe thickness h is predicted to commonly be several decimeters to meters in scale, implying that significant sediment transport can occur when sliding occurs beneath. I adapt theories for the thermodynamic and mechanical balances that control freezing and melting in porous media to determine h as a function of effective stress N , the rate of basal heat flow, and key sediment properties. A fringe is expected only when $N > p_f \approx 1.1 (T_m - T_f)$ MPa/°C, where $T_m - T_f$ is the temperature drop below the pressure-melting point that is needed for ice to infiltrate the pore space; p_f increases with decreased grain size. For sediment properties that are within the typical range expected of the tills beneath glaciers, $p_f = O(10^4)$ Pa. The rate that water can be transported through the fringe and frozen onto or melted from the glacier base can achieve a steady state that is in balance with the rate that latent heat is transported to or from the basal interface. At constant N , when a gradual increase in heat flow from the glacier base causes the rate of melting to decrease, h increases and continues to do so when the heat flow is great enough to produce freezing. As freezing becomes more rapid and h increases further, the rate of fluid supply to the glacier base reaches a maximum when the effective permeability is sufficiently reduced by the partial ice saturation in the fringe. Larger h can be achieved with slower freezing at the glacier base, but steady states with larger h are unstable. The maximum rate of fluid supply to the glacier base is greater at lower N , higher temperature gradients, and for sediments with higher permeabilities. Unsteady behavior can lead to large changes in h when there is a mismatch between the rate that latent heat can be extracted and the rate that fluid is supplied to the glacier base. Transient behavior driven by abrupt changes in N is characterized by rapid variations in freezing rate, followed by slower adjustments to h that are limited by the timescale for the conduction of latent heat. The resulting patterns of sediment deformation are expected to commonly be distributed over finite depth ranges even when shear is perfectly localized at any single instant in time.

Citation: Rempel, A. W. (2008), A theory for ice-till interactions and sediment entrainment beneath glaciers, *J. Geophys. Res.*, *113*, F01013, doi:10.1029/2007JF000870.

1. Introduction

[2] Glaciers and ice sheets are extremely efficient at molding landscapes [e.g., *Hallet et al.*, 1996]. A significant but poorly quantified contribution to their erosive capacity comes from the incorporation of sediments into the basal ice. The processes that control how sediments are frozen onto the glacier base are of central importance to such diverse problems as the formation of Heinrich layers [e.g., *Alley and MacAyeal*, 1994; *Broecker*, 1994; *Hulbe et al.*,

2004], the conditions at ice-stream shear margins [e.g., *Kamb*, 2001; *Raymond*, 1996; *Schoof*, 2004], and the genesis of subglacial landforms. Numerous mechanisms for sediment entrainment have been proposed, some of which are responsible for creating m-scale debris-rich layers (see reviews by *Alley et al.* [1997] and *Knight* [1997]). When the glacier bed and surface are sloped in opposite directions and subglacial water flows upward at a rate that is faster than it can thermally equilibrate with its surroundings, the pressure dependence of the melting temperature can result in glaciohydraulic supercooling. This leads to the formation of frazil ice that entrains suspended sediment and anchor ice that lifts larger clasts from the base of swift-flowing fluid pathways up to where it can be incorporated at the glacier

¹Department of Geological Sciences, University of Oregon, Eugene, Oregon, USA.

base [e.g., *Alley et al.*, 1998; *Roberts et al.*, 2002; *Larson et al.*, 2006].

[3] In places where conditions are not favorable for glaciohydraulic supercooling, different mechanisms for sediment entrainment are required. One such process is suggested by laboratory [*Iverson*, 1993; *Iverson and Semmens*, 1995] and field observations [*Iverson et al.*, 2007] of the transient migration of ice into porous beds as a consequence of pressure-induced regelation. Models of regelation based on the pioneering work of *Philip* [1980] are in reasonable agreement with laboratory and field results and have been combined with treatments of subglacial fluid flow to predict lateral variations in subglacial entrainment [*Iverson*, 2000]. Regelation occurs in response to temperature gradients as well [*Telford and Turner*, 1963; *Gilpin*, 1980; *Dash et al.*, 2006] and is an important ingredient of established models for freezing and frost heave in porous media [e.g., *O'Neill and Miller*, 1985; *Nixon*, 1991; *Fowler and Krantz*, 1994]. An important feature of these models that is not shared by the idealized model of *Philip* [1980] is their prediction of the temperature, or depth, to which regelation can extend both during net melting and freezing at the glacier base. An improved understanding of the underlying physical interactions made possible by experimental and theoretical advances in a number of related fields [e.g., *Dash et al.*, 2006, and references therein] has led to the development of refined frost-heave models that are formulated to accurately account for the effects of the intermolecular forces that are integral to these freezing phenomena [*Rempel et al.*, 2004; *Rempel*, 2007]. Here I adapt these models to describe the thermal and mechanical constraints on the manner in which sediments are incorporated into basal ice that is near the pressure melting temperature and subject to modest levels of effective stress.

[4] The goal is to develop a model for ice-till interactions and sediment entrainment in the simplest possible system that nevertheless retains enough of the essential character of natural glacier environments to provide useful insights. In section 2, I examine the requirements for thermodynamic and mechanical equilibrium at the till-glacier interface. The various components of these requirements are well established and have been considered elsewhere [e.g., *Andersland and Ladanyi*, 2004; *Clarke*, 2005; *Dash*, 1989; *Dash et al.*, 2006; *Paterson*, 1994]. They are brought together here to derive a relationship, equation (11), between the effective stress, the temperature and fluid pressure fields, and the ice distribution at the till-glacier interface. The vertical force balance requires that the effective stress, temperature, and melt rate (through its connection to fluid pressure gradients) must be related in this way. Most of the remainder of the paper is concerned with the special case where ice extends down into the porous subglacial sediments to form a fringe that can move with the glacier when sliding occurs beneath. Section 3 begins with predictions of the steady state fringe thickness as a function of the rate at which ice is frozen to the glacier base, first for the approximate case where the temperature gradient through the fringe is treated as a constant, and then for the more realistic case where the perturbations to the temperature field produced by latent heat release and variations in thermal conductivity are accounted for. The changes in freezing rate and fringe thickness that are predicted in response to changes in effective stress are

presented next. In section 4, I discuss some of the potential implications of these results for a range of glaciological processes that suggest opportunities for further research. Section 5 closes with a few concluding remarks.

2. Balance Conditions at the Till-Glacier Interface

[5] I focus on the basal regions of a glacial system where all variations in the lateral dimensions are sufficiently gradual that a one dimensional treatment is appropriate for describing the balance conditions. It should be possible for those familiar with the ground-freezing literature to skim through this theoretical development and go straight to the glaciological applications discussed in section 3. In porous media, small volumes of liquid water are present at equilibrium over a range of temperatures that are below the normal bulk melting temperature T_m , and the effects of surface energy prevent ice from infiltrating the pore space until the temperature drops below a temperature T_f that is given by equation (3). Standard thermodynamic arguments lead to equation (4) for the equilibrium shape of the ice-liquid interface in the solute-free environment considered here. The geometrical complexities inherent in realistic porous media prompt the use of empirical relationships between ice saturation and temperature of the form given in equation (5). I discuss the connections between these two expressions and how parameters appropriate for different tills can be estimated. With the key geometrical characteristics of the ice-liquid geometry so determined, I examine the vertical force balance and derive equation (11) for mechanical equilibrium at the ice-liquid interface. The special case in which a thick ice-infiltrated fringe develops is described by equation (13), which relates the effective stress to the temperature field, fringe thickness, vertical fluid flow and till characteristics. This is the appropriate generalization of similar expressions that are used to describe the fluid supply during frost heave [e.g., *O'Neill and Miller*, 1985; *Rempel et al.*, 2004; *Rempel*, 2007]. Frost heave is caused by fluid flow toward colder regions, where it freezes in segregated ice lenses that push the overlying material upward as they grow (the density difference between water and ice is of secondary importance). The mechanical and thermodynamic balances that produce fluid flow toward the glacier base are expected to be the same as those that control the fluid supply for frost heave.

2.1. Thermodynamic Equilibrium at Till-Glacier Contacts

[6] Consider a glacier sitting on water-saturated till, with no soluble impurities present. The generalized Clapeyron equation, found by equating the chemical potentials in the liquid and ice at their common interface, requires that

$$p_i - p_l \approx \rho_i \mathcal{L} \frac{T_m - T}{T_m} + (p_l - p_m) \frac{\rho_i - \rho_l}{\rho_l}, \quad (1)$$

where p_i is the ice pressure, p_l is the liquid pressure, T is the temperature, T_m is the bulk melting temperature at reference pressure p_m (e.g., $T_m \approx 273$ K when $p_m = 10^5$ Pa), $\mathcal{L} \approx 3.34 \times 10^5$ J/kg is the latent heat of fusion, and $\rho_i \approx 920$ kg/m³

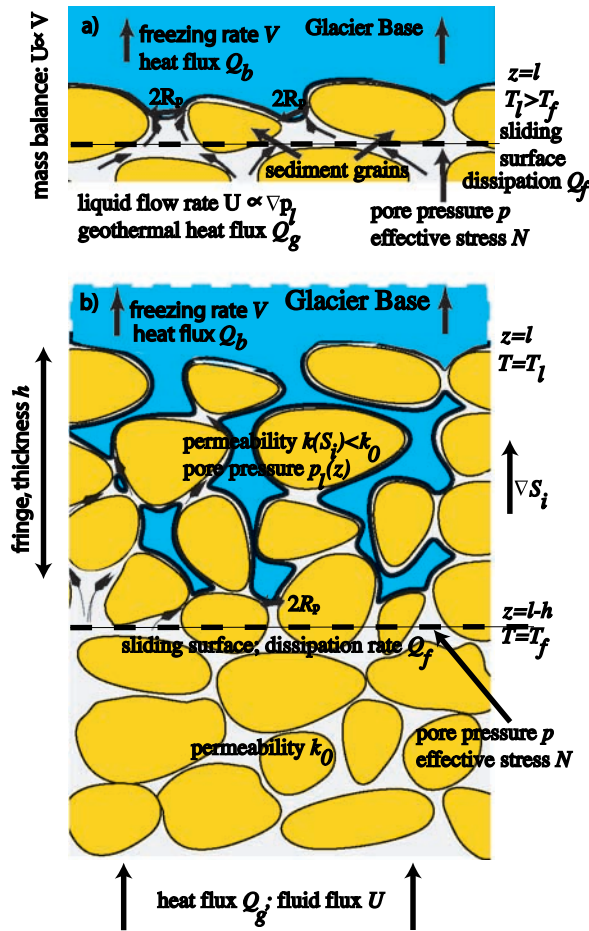


Figure 1. Schematic diagrams of the region near a glacier base (modified from Rempel *et al.* [2004]). In Figure 1a the ice-till interface is sharp, whereas in Figure 1b it is characterized by a fringe with partial ice saturation S_i . In both cases, fluid is shown as flowing toward the glacier base, as is appropriate when freezing is taking place. The liquid flow U can be related to the freezing rate V . The pore fluid pressure p_l is determined by the conservation laws. Sliding is assumed to take place at the farthest extent of pore ice, where the pore pressure is p and the effective stress is N . Frictional dissipation, at rate Q_f , combines with the geothermal heat flux Q_g and latent heat release at a rate proportional to V to determine the basal heat flux Q_b .

and $\rho_l \approx 10^3 \text{ kg/m}^3$ are the ice and liquid densities. Equation (1) holds over any pure ice-liquid interface at equilibrium.

[7] The pressure difference between the ice and liquid can also be related to the specific physical interactions that cause the pressure and temperature state of the ice-liquid interface to deviate from their bulk equilibrium values. For example, in locations where the interface is too distant from till particles to be affected by their presence (i.e., outside the range of intermolecular forces, which typically are important over distances $O(10 \text{ nm})$) the pressure difference between the ice and liquid water is $p_i - p_l = \gamma_{il}\mathcal{K}$, where $\gamma_{il} \approx 0.034 \text{ J/m}^2$ is the interfacial energy of the ice-liquid interface and \mathcal{K} is the curvature; this is the Gibbs-Thomson

effect. Over a flat ice-liquid interface that is distant from any substrates (e.g., when the ice is floating) $p_i = p_l$ and equation (1) describes the pressure dependence of the melting temperature. More generally, when the interface is both curved and interacting with a foreign substrate (e.g., a till particle)

$$p_i - p_l = \gamma_{il}\mathcal{K} + \Pi(d), \quad (2)$$

where the final term describes the dependence of the substrate interactions on film thickness d . The precise functional form of $\Pi(d)$ depends on the nature of the dominant intermolecular forces in the system [Dash *et al.*, 2006], but in all cases $\Pi(d) \rightarrow 0$ as the film thickness gets large in comparison to the range of the forces that act between the ice and the substrate. In the wetting literature $\Pi(d)$ is called the disjoining pressure; this is the force per unit area that the till and ice exert upon each other across a premelted liquid film. For example along a flat interface with $p_i \approx p_m$, equations (1) and (2) indicate that $\Pi(d) \approx \rho_i\mathcal{L}(T_m - T)/T_m \approx 1.1 \times 10^5 \text{ Pa}$ when $T_m - T = 0.1 \text{ K}$.

[8] The interface between till and a glacier can be sharp, in the sense that a zone of essentially pure ice lies atop a zone of liquid-saturated sediments, as shown in Figure 1a. For a till that is characterized by pore throats of radius R_p the maximum curvature of an ice-liquid interface that bridges the gap between adjacent sediment grains is $\mathcal{K} \approx 2/R_p$. Equations (1) and (2) imply that a sharp till-glacier interface is expected when the temperature and liquid pressure in the pore throats adjacent to the ice interface satisfy

$$\rho_i\mathcal{L}\frac{T_m - T}{T_m} + (p_l - p_m)\frac{\rho_i - \rho_l}{\rho_l} \geq \frac{2\gamma_{il}}{R_p},$$

where I have assumed that R_p is sufficiently large that $\Pi(d) \rightarrow 0$ in the center of the pore throats. Typically, the temperature-dependent term on the left is much larger than the term that depends on the liquid pressure. Accordingly, it is useful to identify the temperature T_f that satisfies

$$\rho_i\mathcal{L}\frac{T_m - T_f}{T_m} = \frac{2\gamma_{il}}{R_p}. \quad (3)$$

Figure 1b shows a schematic diagram of the till-glacier interface when the temperature T_l at the base of sediment-free glacier ice is less than T_f so that a fringe of partially frozen sediments extends beneath. In this case, the approximate temperature at the farthest extent of pore ice is T_f , which is treated as a constant that depends only on the geometrical properties of the porous medium. By contrast, T_l is controlled by balance conditions that are described below.

[9] Equations (1) and (2) together imply that

$$\gamma_{il}\mathcal{K} + \Pi(d) \approx \rho_i\mathcal{L}\frac{T_m - T}{T_m} + (p_l - p_m)\frac{\rho_i - \rho_l}{\rho_l}, \quad (4)$$

which in principle can be used to characterize the geometry of the ice-liquid interface within the fringe in terms of its curvature \mathcal{K} and separation from till particles d as a function of the local temperature and liquid pressure. In practice, the complex geometry of the pore space makes direct calcula-

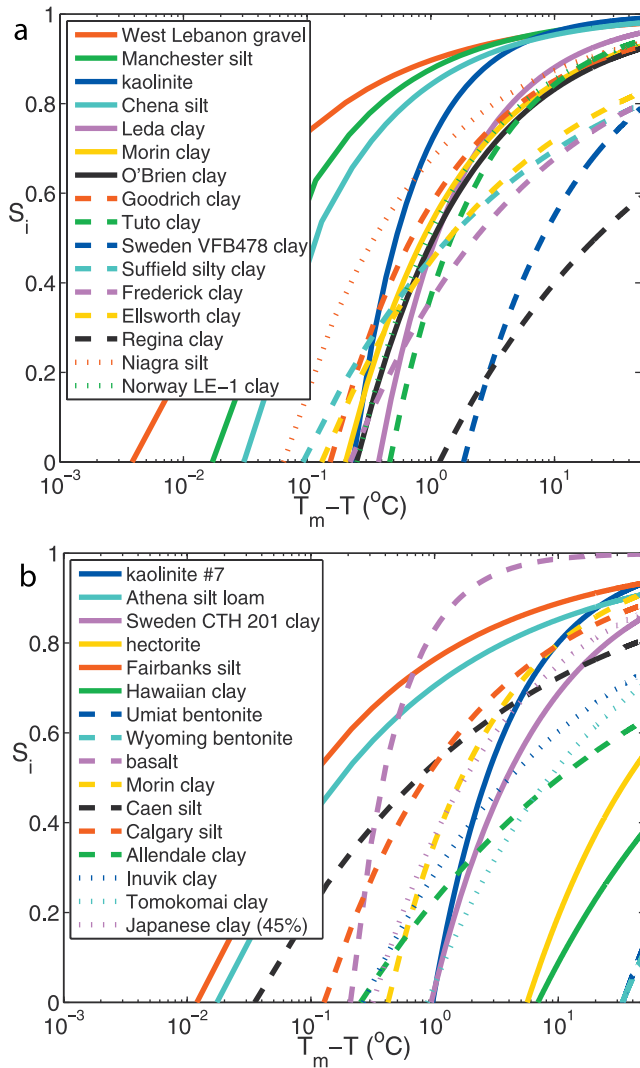


Figure 2. Ice saturation level S_i as a function of the temperature depression from bulk melting $T_m - T$ for different porous media [Andersland and Ladanyi, 2004].

tion of the ice saturation level impractical except in very idealized packing geometries (e.g., for mono-dispersed powders [Cahn *et al.*, 1992; Dash *et al.*, 2006]). Fortunately, the importance of partially frozen sediments to the permafrost community has motivated several empirical studies of the dependence of ice saturation on temperature. Figure 2 shows fits to data giving the volume fraction of pore space filled with ice in many different porous media as a function of $T_m - T$ [Andersland and Ladanyi, 2004]. In each case the dependence of ice saturation on temperature is represented with an empirical relation of the form

$$S_i = 1 - \left(\frac{T_m - T_f}{T_m - T} \right)^\beta. \quad (5)$$

For each porous medium, the horizontal intercept in Figure 2 (i.e., where $S_i = 0$) can be equated with the warmest temperature depression from bulk melting $T_m - T_f$ at

which ice can partially fill the pore space. Consistent with the predictions of equation (3), Figure 2 indicates that T_f tends to be lowest for clays, which are typically characterized by the smallest pore sizes. Whereas the appropriate pore throat radius R_p is difficult to measure directly for realistic, polydispersed porous media, the value of the control parameter T_f can be extracted from empirical data of the type used to generate Figure 2 [e.g., Andersland and Ladanyi, 2004; Nixon, 1991].

[10] For the compilation shown in Figure 2 the exponent β from equation (4) that characterizes the increase in S_i with decreasing temperature varies between 0.19 and 1.15, with a mean of 0.42 (median 0.40) and a standard deviation of 0.20. Theoretical considerations [Cahn *et al.*, 1992] suggest that for a given porous medium β should actually experience a transition between high and low temperature limits that produce changes in the relative importance of the two terms on the right side of equation (2). As the temperature increases toward T_f , most unfrozen liquid is expected to be found in the smallest pores and in pendar rings at particle contacts, where the effective radius of curvature of the ice-liquid interface is inversely proportional to temperature. This suggests that β should tend to a value near 2. At lower temperatures, the water contained within the premelted films that separate the ice from the till particles is expected to control the variation in ice saturation. The relationship between film thickness and temperature is sensitive to the details of the intermolecular interactions that dominate the premelting behavior, with expected values of β at temperatures low enough for films to dominate the liquid fraction ranging between 0.25 and 1 [e.g., Worster and Wettlaufer, 1999]. For example, nonretarded van der Waals forces would be expected to produce $\beta = 1/3$. Experimental constraints may have tended to bias the values for β in Figure 2 toward the lower temperature limit. Clear examples of the transition between the low- and high-temperature saturation regimes are exhibited by experimental data shown in Figures 2–10 of Andersland and Ladanyi [2004] and Figures 2 and 3 of Cahn *et al.* [1992].

[11] I am not aware of any published measurements of the dependence of ice saturation on temperature in glacial tills. With this deficiency in mind, Christoffersen and Tulaczyk [2003] suggested that the specific surface area of sediments might be used to infer aspects of till-freezing behavior. Figure 3 shows measured values of the specific surface area SSA for a subset of the data shown in Figure 2 [Andersland and Ladanyi, 2004] plotted against (Figure 3a) $T_m - T_f$ and (Figure 3b) β . Power-law correlations between these parameters are displayed with dashed lines. In the absence of direct measurements of ice saturation level, such correlations can be used to estimate the shape of the ice saturation function for porous media with known SSA . For example, the till parameters summarized in Table 1 of Christoffersen and Tulaczyk [2003], which are taken to be representative of the sediments beneath Kamb Ice Stream (formerly known as Ice Stream C), correspond to the range of SSA between 28 and 113 m^2/g that is shaded in Figure 3. The power-law correlations shown in Figure 3 suggest ranges for $T_m - T_f$ between 0.018°C and 0.59°C, and β between 0.73 and 0.38 for the low- and high-end values of SSA respectively. Such estimates should be viewed with caution, however, particularly with regards to the exponent β , which appears to tend

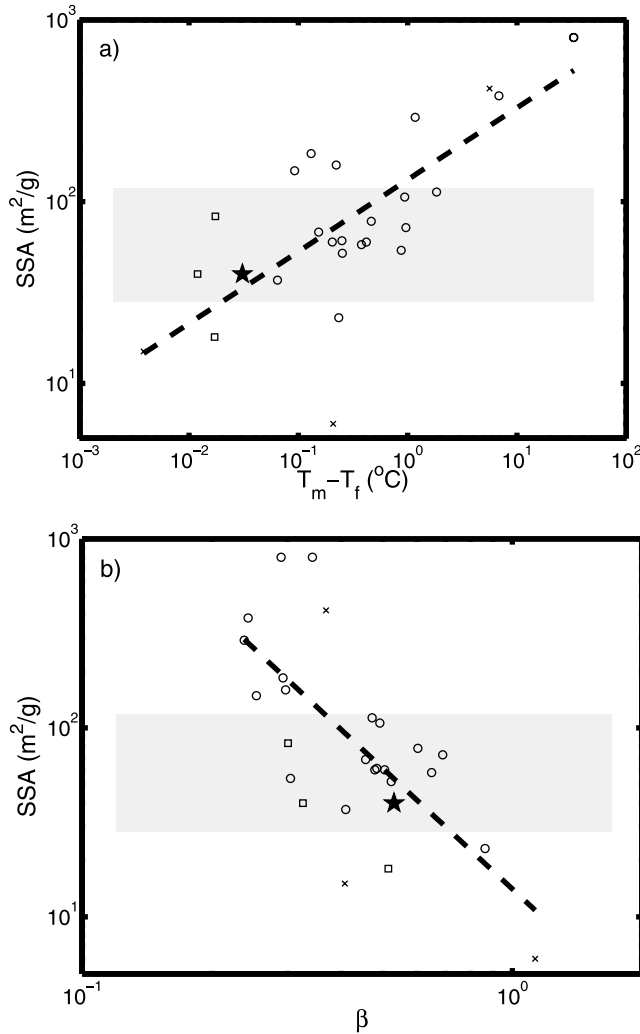


Figure 3. Correlations between specific surface area SSA and (a) $T_m - T_f$ and (b) β for a subset of the porous media with ice saturation data plotted in Figure 2. The circular symbols represent parameters for clays, the squares represent silts and the x's are other types of porous media [Andersland and Ladanyi, 2004], the solid star marks the parameters for Chena silt that are used in the model calculations that follow. Dashed lines show the best-fit power laws, with equations: for Figure 3a, $T_m - T_f \approx 4.3 \times 10^{-6} [SSA/(1 \text{ m}^2/\text{g})]^{2.5} \text{C}$, and for Figure 3b, $\beta \approx 3.5 [SSA/(1 \text{ m}^2/\text{g})]^{-0.47}$.

toward a lower limit at high SSA in Figure 3b. Indeed, the microscopic controls on S_i described above are more consistent with the expectation that β should tend to a constant value rather than follow a power-law dependence on SSA . The correlations reported in Figure 3 should be tested with further direct measurements, especially on glacier tills.

[12] As depicted in Figure 1b, at the glacier base water can flow through the fringe to supply basal freezing or remove meltwater. Ice-infiltrated till can be much less permeable than water-saturated till, so significant pore pressure variations are required to drive such liquid transport. Equation (4) indicates that changes in ice saturation can be caused by variations in liquid pressure as well as temperature. The empirical studies leading to the data fits in

Figure 2 were performed under conditions where the effects of gradients in water pressure were assumed negligible. It is useful to compare the relative importance of these variations by examining the size of the two terms on the right side of equation (4). The effect of liquid pressure variations Δp_l has a negligible influence on the ice-liquid interface geometry in comparison to the effect of temperature variations ΔT when

$$|\Delta T| \gg \frac{(\rho_l - \rho_i)T_m}{\rho_l \rho_i \mathcal{L}} |\Delta p_l| \approx 7 \times 10^{-8} |\Delta p_l| \text{ (K/Pa)}.$$

For changes in p_l of $O(10^5)$ Pa, which are comparable in scale to the ambient effective stresses that pertain beneath glaciers, the ice saturation is thermally controlled as long as changes in T are much greater than 10^{-2} K. In the modeling that follows I assume that S_i is a function of temperature alone and monitor the predicted variations in p_l to make a posteriori assessments of the validity of this assumption.

2.2. Mechanical Equilibrium at Till-Glacier Contacts

[13] The balance of vertical forces on the ice interface at the glacier bed yields a relationship between the temperature at the till-glacier transition and the pore pressure immediately adjacent to the warmest ice. When the till satisfies a Coulomb-plastic rheology and sliding mobilizes the partially frozen fringe, it is this pore pressure that is expected to control the effective stress and the frictional resistance. I take z as positive upward, set the location of the glacier-till interface at $z = l$, and the thickness of partially frozen sediments beneath this level as h (possibly 0). Within the frozen fringe the flow of heat and pore fluid, and the gradients in temperature and pore fluid pressure are assumed to be vertical.

[14] Consistent with the assumptions inherent in formulating a one-dimensional model, I neglect the bridging stresses that may be important in many subglacial environments. Hence the net overburden force per unit area p_0 on the ice-liquid interface is equal to the weight of the overlying ice, which is

$$\begin{aligned} p_0 &= -\rho_i g H - \rho_i g \int_{\text{fringe}} \phi S_i dz \\ &= -\rho_i g (H + h) + \int_{\text{fringe}} (1 - \phi S_i) \rho_i g dz. \end{aligned} \quad (6)$$

Here H is the glacier thickness, g is the acceleration of gravity, and ϕ and S_i are the porosity and the volume fraction of ice in the pore space of the partially frozen fringe. Equation (6) is written so that $p_0 < 0$ to indicate that gravity pushes downward on the ice. When the frozen fringe is absent the downward force per unit area is equal to the glacier weight $p_0 = -\rho_i g H$.

[15] The interactions between the till and ice produce a local force per unit area $\Pi(d)$ that acts in the direction normal to the ice-liquid interface. Considering the ice interface contained within a volume of fringe with constant cross-sectional area A in the horizontal plane, there is no net horizontal force produced by these interactions. However, the net vertical thermomolecular force per unit area between the ice and the till is $p_T = (\int \Pi(d) \hat{n}_z d\Gamma) / A$, where \hat{n}_z is the

vertical component of the outward normal to the ice interface, with area element $d\Gamma$. As shown by *Rempel et al.* [2001] [see also *Rempel et al.*, 2004; *Rempel*, 2007], this force can be calculated as a superposition of the net force that would be exerted on an ice-liquid interface located at the warmest extent of the pore ice (where $z = l - h$), plus the net force that would be exerted against an object that exactly encompasses the region devoid of ice within the frozen fringe, so that

$$p_T = (p_i - p_l)|_{z=l-h} + \int_{\text{fringe}} (1 - \phi S_i) \frac{d}{dz} (p_i - p_l) dz.$$

When the till-glacier interface is sharp and $h = 0$, the integral term disappears and equations (1) and (2) can be substituted for the remaining term on the right to get

$$p_T \approx \rho_i \mathcal{L} \frac{T_m - T_l}{T_m} + (p_l - p_m)|_{z=l} \frac{\rho_i - \rho_l}{\rho_l} = \gamma_{il} \mathcal{K}, \quad (7)$$

where \mathcal{K} is the temperature-dependent curvature of the ice-liquid interface in locations where it is distant from the pore walls (i.e., so that $\Pi(d) \rightarrow 0$), but unable to pass through the pore throats.

[16] When $h \neq 0$, the pressure difference between the ice and liquid at $z = l - h$ can be found from equation (2), and is equal to that caused by the Gibbs-Thomson effect over an interface with curvature \mathcal{K} that is at the threshold of allowing passage through the pore throats. It is worth emphasizing that p_T derives from the integrated effect of ice-till interactions of strength $\Pi(d)$, and thus p_T is not actually produced by the surface energy of the ice-liquid interface. In porous media the effects of surface energy are primarily responsible for setting the upper temperature limit to which pore ice can extend and this determines the thickness d of the premelted films across which intermolecular forces are exerted between the till and the ice.

[17] The gradient in the pressure difference $p_i - p_l$ can be related to the temperature and liquid pressure gradients through equation (1) so that

$$p_T = \gamma_{il} \mathcal{K} - \int_{\text{fringe}} (1 - \phi S_i) \left[\frac{\rho_i \mathcal{L}}{T_m} \frac{dT}{dz} + \left(1 - \frac{\rho_i}{\rho_l}\right) \frac{dp_l}{dz} \right] dz. \quad (8)$$

This is the net force per unit cross-sectional area produced by intermolecular interactions between the glacier and the underlying till.

[18] The distribution of fluid pressures along the ice-liquid interface acts to balance the difference between p_T and p_0 . The net force per unit area that the fluid exerts over the ice-liquid interface can be calculated as $p_\eta = (\int p_l \hat{n}_z d\Gamma) / A$, which I evaluate in a similar manner to p_T as

$$p_\eta = \bar{p}_f + \int_{\text{fringe}} (1 - \phi S_i) \frac{dp_l}{dz} dz, \quad (9)$$

where \bar{p}_f is the average liquid pressure at the base of the partially frozen till. I draw the distinction between the fluid pressure at a particular point on the interface and this average pressure \bar{p}_f in recognition of the fact that there must be some variation to enable flow through restrictions to supply or remove meltwater. When basal melting is occurring, water must flow out from the films that separate the particles from the ice surface so the pressure p in the

water-saturated pores immediately beneath the lowest ice at $z = l - h$ is somewhat lower than \bar{p}_f . The opposite situation arises when freeze-on takes place, and p is somewhat higher than \bar{p}_f . When a frozen fringe is present, these differences are expected to be slight, but they can be significant when the till-glacier interface is sharp. Indeed, the inferred existence of millimeter-scale water layers at the glacier base under circumstances of nonzero effective stress [e.g., *Engelhardt and Kamb*, 1997; *Kamb*, 2001; *Iverson et al.*, 2007] require large differences between the pressure in the water layer and the pressure in the premelted films that intervene between the glacier and weight-bearing larger clasts. As bridging stresses are neglected in the current treatment, I do not consider the presence of such macroscopic water layers further.

[19] The effective stress that is important for frictional resistance depends on p rather than \bar{p}_f , and I define $\delta p = p - \bar{p}_f$ so that δp is negative when melting occurs and flow is away from the interface. The approximate treatment described in Appendix A suggests that

$$\delta p(V, T_l) \approx \frac{\eta R^2 V}{d^3} f(\theta_c),$$

where $\eta \approx 1.8 \times 10^{-3}$ Pa s is the water viscosity, R is the characteristic particle size, V is the rate of freezing (negative if melting), $d(T_l)$ is the average thickness of the premelted films overlying the sediment particles, and $f(\theta_c) = O(1)$ is a function of the average angle θ_c from the particle apex to the point at which the ice interface diverges from the particle surface toward the pore throats. For a film thickness of 10 nm and particles of radius 40 μm , $\delta p \approx 1$ kPa when $V \approx 10$ mm/a.

[20] Combining equations (6), (8) and (9), the vertical force balance over the ice-liquid interface determines p as

$$p = \delta p + \rho_i g(H + h) - \gamma_{il} \mathcal{K} + \int_{\text{fringe}} (1 - \phi S_i) \left(\frac{\rho_i \mathcal{L}}{T_m} \frac{dT}{dz} - \frac{\rho_i}{\rho_l} \frac{dp_l}{dz} - \rho_i g \right) dz. \quad (10)$$

In the limit that $h = 0$, there is no frozen fringe so the integral term disappears and there is a simple relationship between the average fluid pressure at the glacier base, the weight of the overlying ice, and the interfacial curvature in the pore throats far (i.e., $\gg d$) from the till particle surfaces. When the ice is floating and $\mathcal{K} = 0$, \bar{p}_f is determined by the glacier weight. When the ice is not floating, but $h = 0$, equation (10) describes how \mathcal{K} is determined by the difference between the glacier weight and \bar{p}_f . This difference increases as a greater fraction of the glacier weight is supported by intermolecular interactions with the till, and eventually \mathcal{K} becomes sufficiently large that the ice interface penetrates the underlying till to form a fringe with $h > 0$.

[21] When the stress state in the ice is approximately hydrostatic the normal stress σ_n at position $l - h$ is directly proportional to the weight of the overlying material so

$$\sigma_n = \rho_i g(H + h) + (\rho_s - \rho_i) g h + \int_{\text{fringe}} [(\rho_l - \rho_s) g \phi + (\rho_i - \rho_l) g \phi S_i] dz,$$

where ρ_s is the density of till particles. Combining this with equation (10), the effective stress $N = \sigma_n - p$ at the base of the lowest ice is

$$N = \gamma_{il}\mathcal{K} - \delta p - \int_{\text{fringe}} \left[(1 - \phi S_i) \left(\frac{\rho_i \mathcal{L} dT}{T_m dz} - \frac{\rho_i dp_l}{\rho_l dz} \right) - \rho_i g \phi (1 - S_i) - (1 - \phi) \rho_s g \right] dz. \quad (11)$$

This provides a relationship between the effective stress N , the geometry of the ice boundary, the profiles of temperature and fluid pressure, and key characteristics of the porous sediments.

[22] Two special cases are readily identified. First, when $T_l > T_f$ there is no fringe and equation (11) reduces to

$$N = \gamma_{il}\mathcal{K}(T_l) - \delta p(V, T_l), \quad (12)$$

where \mathcal{K} satisfies equation (7). The importance of this regime will be discussed briefly in section 4, whereas the modeling in section 3 is focused on a second limiting case. When $T_l < T_f$, δp typically is expected to be small in comparison to the change in fluid pressure across the fringe. The fluid transport through the fringe is modeled with Darcy's law

$$U = -\frac{k}{\eta} \left(\frac{dp_l}{dz} - \rho_l g \right),$$

where η is the liquid viscosity, k is the ice-saturation-dependent permeability, and U is the Darcy transport rate in the vertical direction that is required to supply freezing (or remove meltwater). Substituting this into equation (11) and using equation (3) to describe the effects of surface energy at $z = l - h$ as $\gamma_{il}\mathcal{K} = 2\gamma_{il}R_p \approx \rho_i \mathcal{L} (T_m - T_f)/T_m$ gives

$$N \approx \rho_i \mathcal{L} \frac{T_m - T_f}{T_m} - \int_{\text{fringe}} \left[(1 - \phi S_i) \left(\frac{\rho_i \mathcal{L} dT}{T_m dz} + \frac{\rho_i \eta}{\rho_l k} U \right) - (\rho_s - \rho_i)g(1 - \phi) - (\rho_l - \rho_i)g\phi(1 - S_i) \right] dz. \quad (13)$$

Equation (13) describes how the effective stress beneath the lowest extent of pore ice is related to the temperature profile and ice saturation throughout the fringe, as well as the fluid supply to or from the glacier base.

3. Consequences for Simple Glacier Systems

[23] When ice extends beneath a glacier to form a partially frozen fringe, the balance conditions just described predict that its thickness h satisfies equation (13), which includes an implicit dependence on h through the integral term on the right. To apply this constraint to realistic glacier systems requires that the temperature field and rate of vertical fluid transport be specified or otherwise determined.

[24] The vertical liquid flow balances the rate of freezing or melting at the glacier base. The ice within the fringe is assumed to regelate at velocity V with respect to the till matrix [e.g., *O'Neill and Miller, 1985*]. I assume that ϕ is constant and

$$\rho_l U = \rho_i (1 - \phi S_i) V \quad (14)$$

throughout the partially frozen zone. For constant freezing rate V this is combined with equation (13) to find that

$$V \approx \frac{\frac{\rho_i \mathcal{L}}{T_m} \left(T_m - T_l + \phi \int_{T_f}^{T_l} S_i dT \right) - [N - (1 - \phi)(\rho_s - \rho_l)gh]}{\frac{\rho_i^2 \eta}{\rho_l^2} \int_{l-h}^l \frac{(1 - \phi S_i)^2}{k} dz}, \quad (15)$$

where the 10% density difference between liquid water and ice has been neglected for the purposes of calculating the weight of material within the partially frozen zone. The first term in the numerator is the net force per unit area that the till particles exert against the ice. This force is controlled by the temperature at the glacier base T_l and the manner in which the ice saturation S_i depends on temperature through the fringe. Importantly, it does not depend on the details of the temperature profile itself. The other term in the numerator is the effective overburden. The hydraulic resistance that determines the pressure distribution required to supply or remove fluid from the glacier base appears in the denominator.

[25] The rheology of debris-laden basal ice is not well understood. In some studies it exhibits characteristics that are "softer" than those of debris-free glacier ice [*Lawson, 1996*], perhaps facilitated by higher liquid contents promoted by the presence of dissolved salts. The results of other studies find no effect on flow rate of sediment concentrations up to 15% by volume [e.g., *Jacka et al., 2003*]. By contrast, deformation tests on frozen sediments from the base of Suess Glacier, Antarctica, indicate a peak shear strength that is nearly twice that of glacier ice samples [*Fitzsimons et al., 2001*]. Fluid dynamics studies of the rheology of particle suspensions find that the effective viscosity increases dramatically above that of the host fluid (i.e., in the present case ice) as particle concentration increases and local shear rates are elevated between nearby solid particles. Here I assume that ice-infiltrated till is sufficiently stiff that negligible deformation occurs within the fringe.

[26] I begin by considering steady state predictions for h at different levels of effective stress N , with V determined from equation (15). To provide intuition for the essential behavior, at first I treat the temperature gradient as constant, and later show how the predictions are modified when the temperature profile is treated in a more realistic fashion. I assume that sliding occurs at a specified rate W_s and treat the till as perfectly plastic so that the slip surface is located at the farthest extent of pore ice. This is the location within the till where the effective stress is lowest, both during melting and at modest freezing rates. For the purposes of calculating the steady state behavior, the precise nature of the resistance to sliding within the till is not crucial (e.g., whether it be plastic or viscous); only the rate at which work is performed and dissipated as "frictional" heat Q_f enters into the calculations. The section closes with a brief discussion of the transient behavior produced by variations in effective stress. The changing fringe thickness that results shares similarities with that predicted by earlier theories for regelation-infiltration into porous sediments [*Philip, 1980; Iverson, 2000*].

3.1. Fringe Thickness for Constant ∇T

[27] Insight into the controls on fringe thickness can be gained by considering the special case where the temperature gradient is constant at $G = -(T_f - T_l)/h$. Equation (15) can be rewritten as

$$V \approx \frac{\rho_l^2 \mathcal{L} G k_0}{\rho_i T_m \eta} \psi(T_l, h) \times \frac{T_m - T_l + \phi \int_{T_f}^{T_l} S_i dT - \frac{T_m}{\rho_i \mathcal{L}} [N - (1 - \phi)(\rho_s - \rho_i)gh]}{\int_{T_f}^{T_l} \frac{(1 - \phi S_i)^2}{k/k_0} dT}, \quad (16)$$

where k_0 is the permeability of the water saturated sediments beneath the farthest extent of pore ice. The function $\psi = 1$ when the temperature gradient through the fringe is constant and more generally

$$\psi(T_l, h) = \frac{\int_{T_f}^{T_l} [(1 - \phi S_i)^2 / k] dT}{G \int_{l-h}^l [(1 - \phi S_i)^2 / k] dz}$$

accounts for the manner in which nonlinearities in the temperature distribution modify the total hydraulic resistance to fluid flow.

[28] A prescription for the variation in permeability with ice saturation or temperature is needed. Data for nine partially frozen fine-grained soils were compiled by *Nixon* [1991] and are reproduced in Figure C-14 of *Andersland and Ladanyi* [2004]. Empirical fits to the data can be expressed in the form

$$k \approx k_0 \left(\frac{T_m - T_f}{T_m - T} \right)^\alpha, \quad (17)$$

where the exponent α characterizes changes to the flow resistance that are produced by the shrinkage of fluid conduits that accompanies freezing. To illustrate this point more clearly, I note that in cases where the ice saturation is described by equation (5) the permeability can also be written as $k \approx k_0 (1 - S_i)^{\alpha/\beta}$. A permeability relationship equivalent to this with α/β between 7 and 9 (based on sparse permeability measurements in a frozen silt) was used by *O'Neill and Miller* [1985] to illustrate their model for frost heave.

[29] For a constant temperature gradient, equation (16) gives an explicit relationship between the freezing rate V , the effective stress N and the fringe thickness h . With the ice saturation described by equation (5) and the permeability described by equation (17), I define the dimensionless undercooling at the glacier base as $\theta_l = (T_m - T_l)/(T_m - T_f) = 1 - Gh/(T_m - T_f)$ and write

$$V \approx V^* \frac{\theta_l + \phi \left[1 - \theta_l + \frac{1}{\beta-1} (1 - \theta_l^{1-\beta}) \right] - \frac{N}{p_f} + \frac{(1-\phi)(\rho_s - \rho_i)gh}{p_f}}{\frac{(1-\phi)^2}{\alpha+1} (\theta_l^{\alpha+1} - 1) + \frac{2(1-\phi)\phi}{\alpha-\beta+1} (\theta_l^{\alpha-\beta+1} - 1) + \frac{\phi^2}{\alpha-2\beta+1} (\theta_l^{\alpha-2\beta+1} - 1)}, \quad (18)$$

where the velocity scale $V^* = -(\rho_l^2 \mathcal{L} G k_0)/(\rho_i T_m \eta) \approx -2.3 \times 10^{15} (G k_0)^\circ \text{C}^{-1} \text{a}^{-1}$, and $p_f = \rho_i \mathcal{L} (T_m - T_f)/T_m \approx 1.1(T_m - T_f)$ MPa/°C. The fringe is absent and the glacier-till interface is

sharp when $N < p_f$. For $N > p_f$ a fringe can be present even when melting takes place. This predicts that coarse-grained tills are most susceptible to basal freeze-on since they are characterized by smaller values of $T_m - T_f$ and lower values of p_f . Note, however, that sliding can be inhibited by the large effective stresses N that tend to accompany thick fringes and large basal undercoolings θ_l .

[30] The current treatment is not designed to apply to cases where the predicted steady state fringe thickness h exceeds the till thickness. Appropriate extensions can be made to deal with such circumstances. For the case where deformable sediments of thickness l overlie a rigid permeable layer, the vertical force balance is not changed significantly when $h > l$, but sliding is expected to be prevented as the fringe is effectively “frozen” to the bedrock. For the case where $h > l$ and the underlying bedrock is impermeable, fluid transport is vanishingly small and a nearly hydrostatic fluid pressure gradient is expected through the fringe. The effective stress at the bedrock interface is balanced by intermolecular interactions across a thin pre-melted film; only very slow sliding is expected under such conditions [e.g., *Shreve*, 1984].

[31] Figure 4 shows the steady state fringe thickness as a function of freezing rate calculated from equation (18) for a number of effective stress values N . The temperature gradient is assumed to be related to the geothermal flux Q_g and the rate of frictional heat production Q_f by $G = -(Q_g + Q_f)/K_e$, where the effective thermal conductivity is $K_e = 2 \text{ W}/(\text{m}^\circ\text{C})$. The till is treated as a Coulomb-plastic material with negligible cohesive strength and friction coefficient $\mu = 0.6$ so that $Q_f = \mu N W_s$. The point where each curve intersects with the dotted line at a freezing rate of $V = 0$ represents the special case where a hydrostatic fluid pressure distribution against the contorted ice surface reduces the effective overburden just enough for ice-till interactions distributed through the fringe thickness h to exactly support the remaining overlying weight; hence the terms in the numerator of equation (18) sum to zero. If h is reduced, the ice-till interactions are no longer sufficient to support the gravitational load so the fluid pressure within the fringe must increase to compensate and the resulting fluid flow away from the glacier base is supplied by melting. By contrast, if h is increased, the net force produced by ice-till interactions exceeds the gravitational load and the fluid pressure drops so that flow toward the glacier base supplies freezing in steady state. As the fringe gets thicker still, eventually the pore space becomes sufficiently clogged with ice that the reduced permeability is prohibitive and V attains a maximum V_{max} before dropping with further increases in h .

[32] For each value of N displayed in Figure 4, h can attain two values at any given $V > 0$ that is less than V_{max} . Of these two, only the smaller h represents a stable steady state.

On the lower branch of each curve, increases (decreases) to h are accompanied by decreases (increases) to V . Small perturbations are destabilizing: when h goes up slightly, V

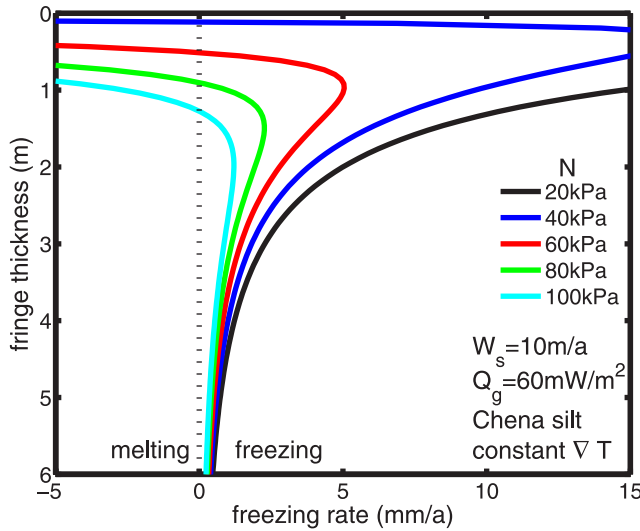


Figure 4. Steady state fringe thickness h as a function of freezing rate V , calculated for the constant gradient approximation from equation (18) for the values of effective stress N noted in the legend. The geothermal gradient is $Q_g = 60 \text{ mW/m}^2$, and the sliding rate is 10 m/a . Soil parameters for Chena silt were used to obtain k and S_i .

drops and so h continues to rise while V gets progressively smaller; when h drops slightly, V goes up and h decreases further until eventually the stable steady state lower h value can be reached. Note that for the case where $N = 20 \text{ kPa}$ the ice-till interactions are strong enough to support the gravitational load with $h = 0$ so only the unstable steady state is shown. Though such unstable steady states are not expected to persist in practice, they do provide some intuition for the transient behavior, as discussed further below. The series of curves shows that higher values of the effective stress require larger h for a given V , and V_{\max} is smaller for larger N .

[33] The calculations for Figure 4 were performed using soil parameters for Chena silt that are based on the behavior reported by *Andersland and Ladanyi* [2004] ($\alpha \approx 3.1$, $\beta \approx 0.53$, $T_m - T_f \approx 0.031^\circ\text{C}$, $k_0 \approx 4.1 \times 10^{-17} \text{ m}^2$ and $\phi \approx 0.35$). While quantitative differences are expected to characterize the behavior of other soils, the overall qualitative behavior just described is expected to be robust. To estimate the stable steady state fringe thickness when only limited knowledge of the till properties is available, the case of $V = 0$ in equation (18) can be used to show that

$$\frac{N - p_f}{(1 - \phi)(\rho_s - \rho_l)g - G\rho_l\mathcal{L}/T_m} \leq h_{V=0} \leq \frac{N - p_f}{(1 - \phi)[(\rho_s - \rho_l)g - G\rho_l L/T_m]}, \quad (19)$$

where the bounds correspond to a fringe with average ice saturation $\bar{S}_i \rightarrow 0$ and $\bar{S}_i \rightarrow 1$, respectively. Because $h_{V=0}$ is less than the fringe thickness at which ice-clogged pores restrict fluid flow sufficiently that $V = V_{\max}$, \bar{S}_i is expected to be closer to zero than unity and the actual steady state value of $h_{V=0}$ is expected normally to be closer to the lower

bound in equation (19). This is the value that would be predicted by the *O'Neill and Miller* [1985] frost-heave model. The terms in the denominators of the left and right sides that represent the effects of gravity (the buoyancy force on the till) and intermolecular forces (the thermodynamic buoyancy [*Rempel et al.*, 2001]), are typically of approximately the same size. The largest stable steady state values of h are expected for coarse-grained tills with $p_f \ll N$. With $G = -(Q_g + Q_f)/K_e$ equation (19) gives $0.06 \text{ m/kPa} \leq h_{V=0} = \phi(N - p_f) \leq 0.07 \text{ m/kPa}$ when $\phi = 0.35$, $\rho_s = 2650 \text{ kg/m}^3$, $K_e = 2 \text{ W/(m}^\circ\text{C)}$, and $Q_g + Q_f = 0.1 \text{ W/m}^2$.

3.2. Steady State Fringe Thickness With Spatially Varying ∇T

[34] As ice grows or melts near the glacier base, the temperature profile in the partially frozen fringe is perturbed by latent heat effects and the constant gradient approximation leads to inaccuracies (e.g., $\psi \neq 1$ in equation (16)). For an improved treatment, I consider more carefully the simple model system depicted in Figure 1b. Till is in contact with a continuous layer of glacier ice at $z = l$. A region of connected pore ice extends downward to form a fringe of thickness h . Sliding at rate W_s occurs along a surface immediately beneath the farthest extent of pore ice. I begin by seeking steady state solutions to the model equations for an imposed effective stress N and geothermal heat flux $-Q_g$. More realistically, one can view N as being determined by larger-scale drainage conditions and hydrological requirements at the glacier base. Some effects of transient changes in N will be examined later. The geothermal flux is treated as constant since it is typically expected to undergo variations over timescales that are much longer than those considered here.

[35] The heat balance through the partially frozen till is approximated from equation (B6), which is derived in Appendix B. Using equation (5) to describe the ice saturation behavior, the one-dimensional, steady state temperature equation can be written as

$$\frac{\phi\beta}{T_m - T_f} \left(\frac{T_m - T_f}{T_m - T} \right)^{\beta+1} \frac{dT}{dz} \left[\rho_l \mathcal{L} V + K_e \ln \left(\frac{K_i}{K_l} \right) \frac{dT}{dz} \right] \approx K_e \frac{d^2 T}{dz^2}. \quad (20)$$

Here K_i and K_l are the thermal conductivities of the ice and liquid water, and the overall effective thermal conductivity in the fringe K_e is calculated as a function of the ice saturation level from equation (B5). As in the approximate treatment, I assume that frictional work augments the heat transport into the fringe from below so that

$$\left. \frac{dT}{dz} \right|_{(l-h)^+} = -\frac{Q_g + Q_f}{K_e}, \quad (21)$$

where the rate of frictional heat production is $Q_f = \mu N W_s$ and the geothermal heat flux $-Q_g$ is assumed fixed. I use this gradient and the known temperature T_f at $z = l - h$ as initial conditions and integrate equation (20) to $z = l$ using the results from the constant-gradient approximation for an initial estimate of the steady state freezing rate V at a particular value of h . The temperature profile that results is used to evaluate ψ and equation (16) then yields a revised

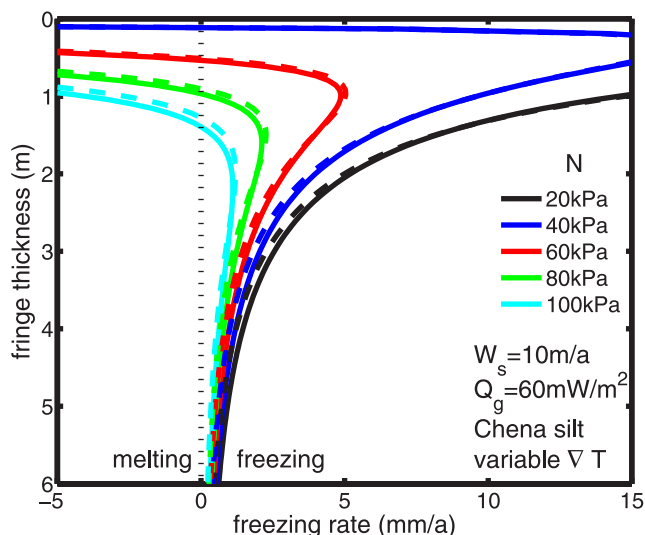


Figure 5. Steady state fringe thickness h as a function of freezing rate V , calculated while accounting for spatial variations in the temperature gradient. Dashed lines display the constant- ∇T results of Figure 4 for comparison. The values of effective stress N are noted in the legend. The geothermal gradient is $Q_g = 60 \text{ mW/m}^2$, and the sliding rate is 10 m/a . Soil parameters for Chena silt were used to obtain k and S_f .

estimate of the freezing rate. I use the revised V to repeat the integration in an iterative procedure that continues until further changes in V are negligible.

[36] Figure 5 shows h as a function of V for the case where the till is described using the saturation and permeability functions of Chena silt and the same range of effective stresses that were used to obtain the results of the constant-gradient approximation shown in Figure 4. As expected, the qualitative behavior is not changed significantly,

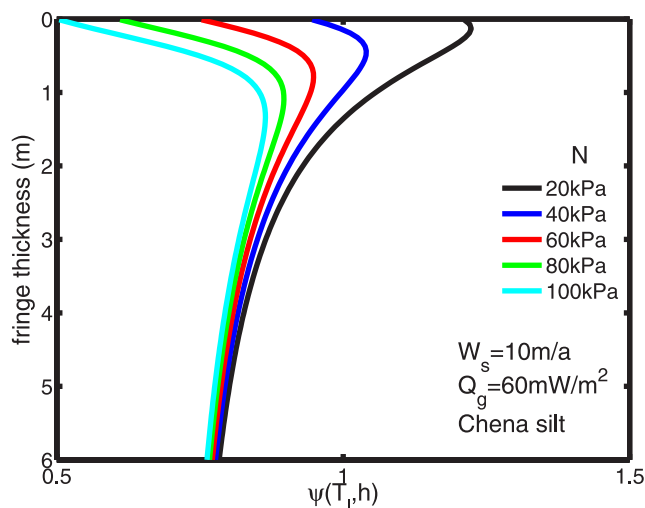


Figure 6. The $\psi(T_l, h)$ as a function of h . This is the factor by which the magnitude of the predicted freezing rate in Figure 5 for the calculated temperature profile exceeds that which would be predicted for a constant temperature gradient of $(T_l - T_f)/h$.

though the quantitative results are altered somewhat. Figure 6 illustrates these differences by showing the factor $\psi(T_l, h)$ by which the magnitude of the freezing rate is increased relative to the predictions of the constant gradient approximation. Though ψ varies with h and is sensitive to the other control parameters as well (such as N), it remains close to unity. Given the other uncertainties involved in describing realistic subglacial conditions, for many applications it may suffice to use the constant gradient approximation (perhaps incorporating a reasonable estimate for the value of ψ or the dependence of ψ on h), thus avoiding the effort of solving the boundary value problem for the temperature field.

[37] The effect of changing the rate of frictional heating by altering the rate of glacier sliding W_s is shown in Figure 7. Equation (21) requires that the magnitude of the temperature gradient at the fringe base increases at higher sliding rates. This causes decreases in the thicknesses of the premelted films to occur over a shorter vertical length scale and the ice-till interactions are able to support the required load with lower values of h . At the same time, the reduction in the hydraulic path length causes the maximum rate of freezing for a given N to increase with W_s .

3.3. Transient Behavior

[38] Values of the steady state fringe thickness for a given sliding rate and effective stress may be useful for assessing subglacial sediment transport patterns over long time periods. It is clear, however, that W_s and N are actually dynamic quantities. The steady state calculations suggest that changes to these control variables should cause adjustments to both the fringe thickness and the rate of basal freezing (or melting). The speed with which h can adjust is limited by latent heat effects that perturb the thermal field near the

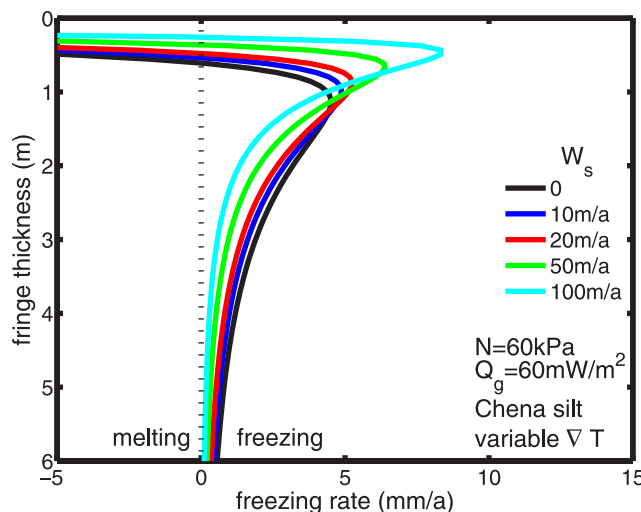


Figure 7. Fringe thickness as a function of freezing rate for $N = 60 \text{ kPa}$ and the different sliding rates W_s noted in the legend. The highest peak freezing rate shown occurs for $W_s = 100 \text{ m/a}$. The rate of frictional heat production is $Q_f = \mu N W_s$, so faster sliding rates correspond to higher temperature gradients near the glacier bed. With $\mu = 0.6$ and $N = 60 \text{ kPa}$, for $W_s = 10, 20, 50,$ and 100 m/a , $Q_f \approx 11, 23, 57,$ and 114 mW/m^2 , respectively.

glacier base so that it relaxes onto a new steady state on the timescale for conduction of latent heat. The pore fluid pressure can adjust more rapidly and produce consequent changes in V . Referring to Figures 5 and 7, I expect the transient evolution following a change in N or W_s to be characterized by a rapid change in freezing rate V with very little immediate modification to the fringe thickness h (i.e., a horizontal path on either of these plots), followed by more gradual changes to both h and V (i.e., along a similar path to the trace of the steady state curve for the new value of N or W_s), potentially leading eventually to a new steady state configuration. To make this intuition more precise requires an examination of the transient thermal evolution.

[39] It is necessary to consider the heat transport within layers on either side of the fringe in order to calculate the transient response to changes in sliding rate or effective stress. I consider a lower layer of thickness $l - h$, which is thick enough that changes to the thermal field are negligible at its base (i.e., thicker than the thermal diffusion length $\sqrt{\kappa_u t_{\max}}$, where $\kappa_u = K_u/(\bar{\rho}c_u)$ is the thermal diffusivity and t_{\max} is the duration of the calculation or the time to adjust to a new steady state). At the base of this layer, I impose a constant geothermal heat flux $-Q_g$. Its top is marked by the moving boundary where the temperature $T = T_f$. Within the layer, the temperature field satisfies the diffusion equation

$$\bar{\rho}c_u \frac{\partial T}{\partial t} = K_u \frac{\partial^2 T}{\partial z^2}, \quad (22)$$

where $\bar{\rho}c_u$ and K_u are the heat capacity and thermal conductivity of the unfrozen till mixture.

[40] I also need to consider a layer that extends up into the glacier above the fringe. At the base of this layer, latent heat release contributes to an increase in the heat flux above that in the fringe below. I make the layer thick enough that the heat flux at its upper surface remains constant at the value dictated by the initial thermal field, which I assume was in steady state prior to the perturbation at $t = 0$. The temperature evolves within the lower reaches of this layer by diffusion so that

$$\rho_i c_i \frac{\partial T}{\partial t} = K_i \frac{\partial^2 T}{\partial z^2}, \quad (23)$$

where $\rho_i c_i$ and K_i are the heat capacity and thermal conductivity of the ice.

[41] In the fringe itself, the temperature evolves by a combination of conduction and latent heat release. Following the derivation in Appendix B and using equation (5) to describe the variation in ice saturation with temperature and equation (B5) to describe the variation in effective conductivity K_e with ice saturation, the leading order heat balance from equation (B4) is written as

$$\begin{aligned} \frac{\partial T}{\partial t} + \left[V + \frac{K_e}{\rho_i \mathcal{L}} \ln\left(\frac{K_i}{K_l}\right) \frac{\partial T}{\partial z} \right] \frac{\partial T}{\partial z} \\ \approx \frac{T_m - T_f}{\phi \beta \rho_i \mathcal{L}} \left(\frac{T_m - T}{T_m - T_f} \right)^{\beta+1} K_e \frac{\partial^2 T}{\partial z^2}. \end{aligned} \quad (24)$$

where V is determined from equation (15). The timescale for conduction of latent heat within the fringe can be compared

to the timescale for conduction of sensible heat in the unfrozen till and ice to a similar distance on either side. Scaling arguments suggest that the right sides of equations (22)–(24) balance the terms involving the time derivatives when $\Delta t_u = (\Delta z)^2 \bar{\rho}c_u/K_u \approx \Delta t_i = (\Delta z)^2 \rho_i c_i/K_i \ll \Delta t_f = (\Delta z)^2 \phi \beta \rho_i \mathcal{L}/[K_e(T_m - T_f)]$. For example with $\Delta z = 0.6$ m, $\Delta t_u \approx 6$ days, $\Delta t_i \approx 4$ days, and $\Delta t_f \approx 10$ years. As an alternative to following the procedure described here, the more rapid diffusive adjustments on either side of the fringe suggest that the current three-layer model can be approximated well by fixing the temperature gradient on either side of the fringe and solving equation (24) subject to these modified boundary conditions.

[42] At the base of the fringe, the temperature and heat flux are both set, the latter by a jump relative to that in the underlying layer. This lower boundary is free to move. At the top of the fringe, the heat flux is related to that in the overlying layer and continuity is required of the temperature at the boundary itself. The mechanical integral constraint from equation (16) must be satisfied as well. The solution strategy involves first transforming the equations into stretched variables to fix the location of the fringe base, where $T = T_f$. Imposing the boundary conditions at this location gives the rate of interface motion as

$$\begin{aligned} \left(\frac{\partial T}{\partial z} \Big|_{z=(l-h)^-} - \frac{Q_f}{K_e} \right) \frac{dh}{dt} \\ = \left\{ \frac{K_e(T_m - T_f)}{\phi \beta \rho_i \mathcal{L}} \frac{\partial^2 T}{\partial z^2} - \left[V + \frac{K_e}{\rho_i \mathcal{L}} \ln\left(\frac{K_i}{K_l}\right) \frac{\partial T}{\partial z} \right] \frac{\partial T}{\partial z} \right\} \Big|_{z=(l-h)^+}. \end{aligned} \quad (25)$$

Because the ice saturation is assumed to change smoothly from $S_f = 0$ at the fringe boundary, equation (25) does not include a jump in heat flux due to latent heat effects, but frictional heating associated with sliding immediately beneath the fringe is represented. Further details of the numerical procedure are discussed in Appendix C.

3.3.1. Response to Changes in N

[43] Figures 8 and 9 show how the freezing rate and fringe thickness respond to rapid changes in the effective stress. The steady state predictions from Figure 5 are shown for reference as dashed curves in Figure 8. The temperature field was initially set to a steady state with $N_0 = 60$ kPa and $h_0 = 0.6$ m so that $V_0 \approx 2$ mm/a (marked in Figure 8 with a solid star). Drops in N of 40 and 20 kPa (two sets of curves with V increasing initially, black and blue), and increases in N of 20 and 40 kPa (two sets of curves with V decreasing initially, green and cyan) were then imposed over a 1-day time period. In each case, to satisfy the force-balance constraint the distribution of fluid pressure within the fringe responded immediately to the change in effective stress. For example, increases in N are accompanied by drops in p at $z = l - h$, which cause the pressure gradient across the fringe to be reduced and drive slower fluid transport; the freezing rate adjusts accordingly, as shown in the inset to Figure 9a. With N held fixed at its new value, the short-term response in each case was similar. The large transient changes in freezing rate caused significant adjustments to the thermal field within the fringe because of latent heat effects; these produce cooling when V decreases and heating when V increases.

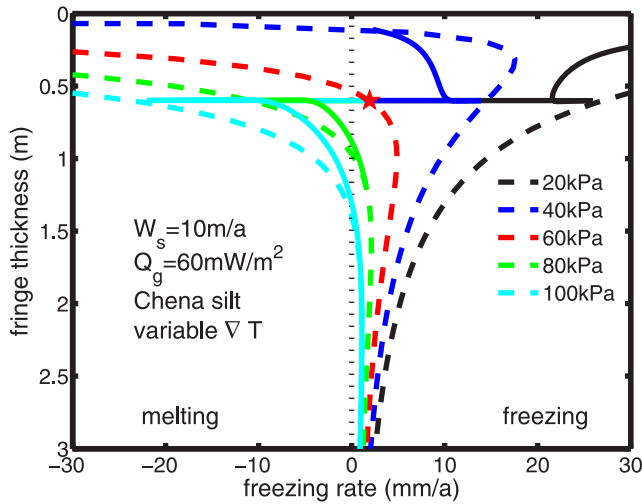


Figure 8. Evolution of h and V from the initial steady state marked by the solid star ($h_0 = 0.6$ m, $V_0 \approx 2$ mm/a, $N_0 = 60$ kPa). The solid curves show responses to rapid changes in N of -40 , -20 , $+20$, and $+40$ kPa; N was subsequently held fixed at its new value (i.e., 20, 40, 80, and 100 kPa). Calculations were extended until either (1) the fringe disappeared (black curve, far right $\Delta N = -40$ kPa), (2) the system achieved a new steady state (blue and green curves, $\Delta N = +20$ and -20 kPa), or (3) long-term fringe growth was indicated by the system evolution coinciding with a sequence of unstable steady states (cyan curve, far left, $\Delta N = 40$ kPa). Dashed curves repeat the information given in Figure 5, and show steady state predictions for the initial and final values of effective stress.

Those systems that had experienced drops (increases) in N followed the increases (decreases) in V by slight increases (decreases) in h over a period of approximately 4 months (see the inset to Figure 9b) as V began to relax back toward its initial value. By this time the perturbed thermal field had adjusted to cause a significant decrease (increase) in heat transport and pore ice began to melt (freeze) at the base of the fringe so that h began to drop (increase). After this initial period, three different types of behavior were identified over the following 5000 years of model time as the temperature profile and fringe thickness adjusted further. The fringe either (1) was lost completely, (2) evolved to a new steady state, or (3) grew indefinitely; brief descriptions follow.

[44] 1. For the case where N dropped to 20 kPa (black curve, far right of Figure 8), after about 1 year of model time had elapsed, the temperature at the glacier base T_b had cooled sufficiently that the resulting increase in net thermomolecular force required further changes to the fluid pressure distribution, with p_f decreasing at the top of the fringe. This caused increases in V that were compounded by the reduced hydraulic path length that accompanied decreases in h . The rate of drop in h accelerated and the entire fringe disappeared after a total elapsed time of approximately 1 year and 8 months, upon which calculations were terminated. Since $p_f > 20$ kPa, the stable steady state fringe thickness for this value of N is $h = 0$.

[45] 2. For the two cases where N was changed by 20 kPa, both the adjustments to V that began once N reached its new steady value, and the adjustments to h that were initiated after 4 months, continued to progress in the same direction until new stable steady states were reached. This took approximately 5 years of model time for the drop to 40 kPa and 200 years of model time for the increase to 80 kPa. The final freezing rates were just sufficient to restore the heat flux through the fringe to its initial value following the changes in rate of frictional heat generation that accompanied the changes in N . As shown in Figure 8, for these cases the final

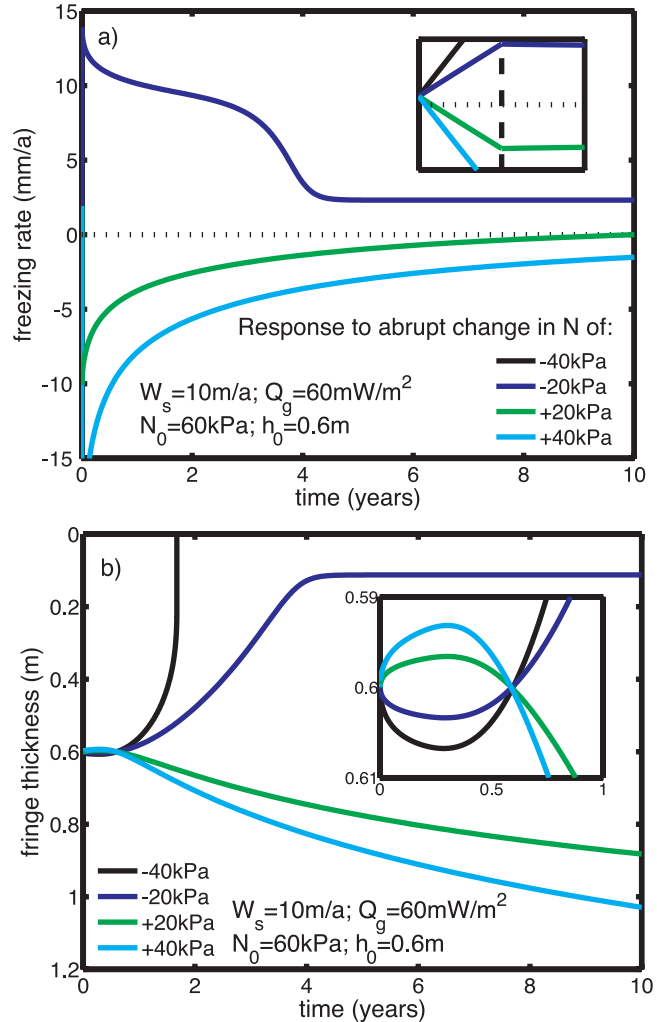


Figure 9. Transient evolution following steady changes in N over a 1-day period (values noted in the legend, from -40 kPa for the top, black curves to $+40$ kPa for the bottom, cyan curves). (a) Changes in freezing rate with time; the dashed line in the inset corresponds to 1 day (the range of the vertical axis is the same as for the main plot, with the initial freezing rate approximately 2 mm/a), after which the changes in N are complete and the system slowly adjusts. (b) Changes in fringe thickness with time; the inset is a magnification of the system response during the first year, with the h scale ranging from 0.61 to 0.59 m. Note that the calculations for N dropping by 40 kPa (black) lead to the disappearance of the fringe in under 2 years.

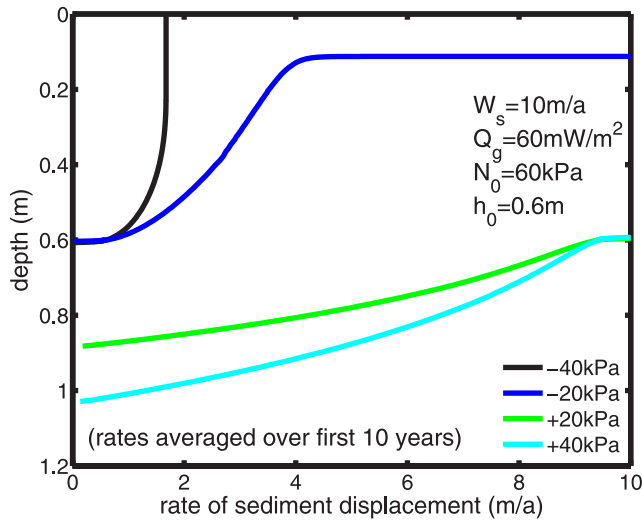


Figure 10. Rate of displacement as a function of depth within the till beneath the glacier, averaged over the first 10 years of transient evolution shown in Figures 8 and 9. The magnitudes of the changes in N range from a drop of -40 kPa for the top curve to $+40$ kPa for the bottom curve, as noted in the legend.

values of h and V lie on the stable upper branches of the steady state predictions from Figure 5.

[46] 3. For the case where N was increased to 100 kPa (cyan curve, far left of Figure 8), the path of changes in V and h also brought the system onto the corresponding steady state curve. In this case, however, the rate of latent heat release required to restore the heat flux to its initial value was incompatible with the maximum rate that fluid could be supplied through the fringe. Continued freezing caused the fringe thickness to increase instead, reaching approximately 10 m by the end of the 5000-year model calculation. In addition, the temperature at any given point within the fringe became progressively colder and the ice saturation steadily increased.

[47] Note that the initial responses to the effective stress increases simulated here actually involve changes to the direction of subglacial flow within the fringe, so that periods of net melting occur. Once the temperature at the glacier base decreases sufficiently for ice-till interactions to produce a net force that exceeds the gravitational load, the flow direction reverses again and net freezing resumes. The responses to decreases in N included substantial increases to V that would be expected to lift the glacier by amounts on the order of 2–4 cm for the two sets of calculations described here.

[48] Figure 10 shows the rate of sediment displacement within the till averaged over the first decade of the simulations shown in Figures 8 and 9. Distributed deformation that occurs over an extended time period is the integrated effect of localized deformation at the base of a fringe of time-varying thickness. However, it is possible that such deformation profiles could be mistaken for evidence that deformation is distributed at a particular instant in time. Till rheology has been the subject of vigorous debate [see, e.g., Hindmarsh, 1997; Kamb, 2001; Tulaczyk *et al.*, 2000; Iverson and Iverson, 2000; Iverson *et al.*, 2007]. Other

mechanisms for causing a zone of localized plastic deformation to migrate within a finite depth range have been suggested previously. These include the breaking of force chains [Iverson and Iverson, 2000], shear-induced dilation [Iverson *et al.*, 1998], and changes in the position of minimum N that accompany transients in fluid flow within compressible tills [e.g., Tulaczyk *et al.*, 2000; Kavanaugh and Clarke, 2006]. The results presented here provide yet another mechanism for distributed deformation in a plastic till, in this case even when the compressibility is negligible. Moreover, it is worth mentioning once again that uncertainties in the rheology of ice-infiltrated till [e.g., Lawson, 1996; Fitzsimons *et al.*, 2001; Jacka *et al.*, 2003] leave open the possibility that deformation may occur within the fringe itself, most likely in a viscous fashion.

[49] It should be noted that for sufficiently high freezing rates, further analysis shows that the effective stress can actually attain a minimum within the till some distance beneath the fringe base rather than at the fringe base itself. This situation, which suggests that sometimes sliding may not be localized to the fringe boundary as has been assumed here, is expected to arise when $V > (\rho_s - \rho_l)(1 - \phi) g \rho_l k_0 / (\rho_l \eta) \approx 8.4$ mm/a for the nominal parameter values. Without accounting for the effects of compressibility or lateral water migration in the unfrozen till, this minimum would be expected to either reach $N = 0$ or occur at the base of the unfrozen permeable layer. More realistic predictions for the location of minimum N within the till during rapid freezing require a more detailed model that includes the changes in fluid pressure produced by horizontal fluid flow in the unfrozen till and the influence of poroelastic effects. Such complications are beyond the scope of the current work, but certainly do merit further consideration. It should be emphasized that the location of frictional dissipation within the unfrozen till does not influence the steady state behavior. Moreover, because the timescale for temperature adjustments in the unfrozen zone Δt_u is so much less than the timescale for temperature adjustments in the fringe Δt_f , the influence of sliding location on the transient behavior is expected to be small as well. The sliding location does influence profiles of displacement with depth, however. The profiles shown in Figure 10 were calculated under the assumption that the sliding surface remained localized at the fringe base; a more advanced model might be expected to predict otherwise for the highest freezing rates produced in response to drops in effective stress, as shown in Figures 8 and 9.

4. Discussion

[50] Well-established thermodynamic principles predict the equilibrium temperature of an ice-liquid interface as a function of its shape and proximity to sediment particles. When combined with an analysis of the vertical force balance, m-scale layers of ice-infiltrated sediments are predicted to extend beneath glaciers under relevant conditions of effective stress N and heat transport. When N is high enough, such layers are predicted to persist even when net melting occurs at the glacier base. This is a coupled system in which changes in N or sliding rate W_s are expected to produce changes in fringe thickness h and freezing rate V . In particular, larger h is expected to result

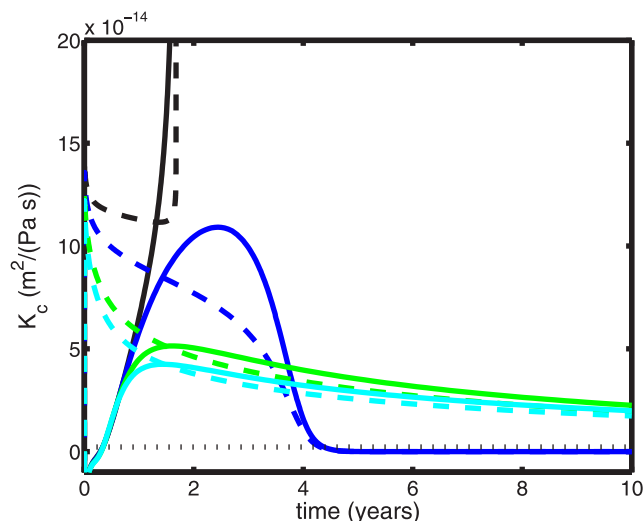


Figure 11. Apparent conductivity of the sediments to ice infiltration for the transient calculations shown in Figure 9. Solid curves use the same color-coding as before, with black and blue (highest pair of curves) corresponding to drops of 40 and 20 kPa, and green and cyan to increases of 20 and 40 kPa, respectively. The dotted line shows the theoretical value of K_c from Philip's [1980] regelation theory. Dashed curves are the apparent conductivity obtained from the approximate fringe growth rate of equation (26).

from higher N or slower W_s . Certain sediment properties play a key role as well. Of particular importance are the dependence of ice saturation S_i and permeability k on temperature. This is illustrated by the parameters p_f and V^* that were introduced in equation (18). For example, the effective stress that must be exceeded for ice to first infiltrate the sediments p_f increases for finer grained sediments as a result of surface-energy effects that cause the temperature of ice infiltration T_f to decrease. The velocity scale V^* that characterizes the rate at which liquid can be supplied through the frozen fringe is directly proportional to the permeability of the ice-free sediments k_0 .

[51] The dependence of freezing behavior on properties of the underlying sediment greatly complicates the task of modeling the ensuing glacial sediment transport in a realistic fashion. As noted earlier, further data are required on the dependence of ice saturation and permeability on temperature in glacier tills. Some general statements can nevertheless be made. Sediments dominated by coarse-grained particles are expected to first be infiltrated by ice at lower N than is required for ice infiltration into more fine-grained sediments. If sliding is initiated in an originally stagnant region, for example after N decreases below a critical level, sediments that are contained within the fringe can be moved together as a package, or raft, quite possibly avoiding significant deformation. If a fringe dominated by coarse-grained sediments is slid on top of fine-grained sediments, the effective stress can decrease substantially before coarse-grained particles are deposited; conversely, the effective stress must increase substantially before the fine-grained particles are entrained. If a fringe dominated by fine-grained sediments is slid overtop of coarse-grained

sediments, the fringe can thicken without requiring any change in effective stress. If fine-grained particles are concentrated at the sliding interface [e.g., *Kamb*, 2001], they can control T_f and limit the ability of the fringe to infiltrate further. This suggests a potential mechanism for causing substantial supercooling in larger underlying pores, so that disconnected ice might be nucleated and modify the resistance to fluid flow, perhaps leading to changes in heat flow that facilitate later ice growth and eventual assimilation to the fringe; such complications are beyond the scope of the current investigation.

[52] When subject to a perturbation, the fringe thickness can grow considerably over decadal timescales, as illustrated by the transient calculations shown in Figure 9. The details of the mechanism for fringe growth and the parameter regime considered here are somewhat different from those treated theoretically by Philip [1980] and examined experimentally by Iverson [1993], Iverson and Semmens [1995], and Iverson *et al.* [2007]. In particular, as mentioned in the discussion surrounding equation (19), the effects of interfacial premelting are approximately as important as the effects of forces due to gravity, whereas they are neglected in Philip's [1980] theory. Moreover, the magnitude of the heat flow considered in the transient calculations here is sufficient to cause net freezing rather than allow net melting, and the changes in effective stress are much lower than those imposed in any previous experimental work. With these differences in mind, it is nevertheless useful to compare results in terms of the apparent conductivity K_c of the fringe matrix to ice infiltration driven by changes in effective stress ΔN . Following equations (1)–(4) of Iverson and Semmens [1995], I evaluate $K_c \approx (hdh/dt)/\Delta N$ for the calculations shown in Figure 9, and compare with the calculated value of $2.2 \times 10^{-15} \text{ m}^2/(\text{Pa s})$ expected from Philip's [1980] theory. As shown by the color-coded solid curves in Figure 11, despite differences in the size and sign of dh/dt between the different modeling scenarios examined in Figures 8 and 9, the apparent conductivity of the sediments to ice shows similar trends in the early stages of each calculation. For a short time at first the rate of fringe thickening is opposite to the direction of the effective stress change and K_c is negative because of the adjustment to the thermal field produced by latent heat effects that were discussed in section 3.3. Subsequently, dh/dt changes sign and K_c increases quickly to surpass Philip's prediction by more than an order of magnitude in each case. The faster rate of fringe growth is promoted in the current model both by a background heat flux that is sufficient to accommodate freezing in the initial steady state, and by the partial ice saturation, which allows for changes in h without freezing or melting the entire pore volume. The rate of change to K_c begins to slow later and, except for the case where the fringe disappears, K_c starts to decrease within the first few years.

[53] An expression for the approximate rate of fringe growth can be obtained by considering the heat balance across the fringe during its transient evolution. If changes are sufficiently slow, the basal heat flux Q_b into the glacier ice should carry away the sum of the geothermal Q_g and frictional Q_f heat fluxes as well as the net latent heat from melting or freezing, which produces a heat flux of $\rho_i \mathcal{L} [V + \phi d(h \bar{S}_i)/dt]$ where $\bar{S}_i = (\int S_i dz)/h$ is the average ice saturation in the fringe. Though the thermal profile in the fringe is nonlinear and time varying, S_i is approximated

while treating the temperature gradient as uniform and equal to $G = -(Q_g + Q_f)/K_u$ so that the heat balance gives

$$\frac{dh}{dt} \approx \frac{Q_b - (Q_g + Q_f + \rho_i \mathcal{L}V)}{\rho_i \mathcal{L} \phi \left[1 - (1 - hG/(T_m - T_f))^{-\beta} \right]}$$

where $Q_f = \mu(N_0 + \Delta N)W_s$ with N_0 the initial value, and Q_b and V are the transient values. As noted earlier, latent heat effects cause the timescale for temperature changes in the fringe Δt_f to be much longer than the thermal diffusion timescale in the ice Δt_i (i.e., the Stefan number is large). As a consequence Q_b is nearly constant and a further approximation gives

$$\frac{dh}{dt} \approx \frac{-\mu \Delta N W_s + \rho_i \mathcal{L}(V_0 - V)}{\rho_i \mathcal{L} \phi \left[1 - (1 - hG/(T_m - T_f))^{-\beta} \right]}, \quad (26)$$

where V_0 is the initial freezing rate. The dashed curves in Figure 11 show K_c obtained for dh/dt calculated from equation (26). At short times equation (26) does a poor job at predicting the rate of fringe growth because the ice distribution within the fringe is able to adjust in response to the change in N and rapid variations in dh/dt are not required. However, the relatively good agreement between the predictions of equation (26) and the transient calculations at times exceeding 4 years suggests an encouraging avenue for further exploration in models that are concerned with long-term patterns of erosion by glaciers and ice sheets.

[54] When h is greater than the value for which $V = V_{\max}$, the steady states shown in the lower portions of Figures 5 and 7 are not stable and the rate of fluid supply to the glacier base is expected to change through time. If latent heat is extracted more rapidly than fluid can be supplied, the fringe thickness can easily reach several meters given sufficient time. An example of such behavior was illustrated by the transient calculation in section 3.2 for N increasing by 40 kPa to 100 kPa. This suggests that increases in basal heat flow or effective stress that cause the rate of freezing to exceed V_{\max} can lead to prolonged sediment accretion that may contribute toward the sediment loading required to explain Heinrich events [e.g., *Alley and MacAyeal*, 1994; *Broecker*, 1994; *Hulbe et al.*, 2004]. Spatial variations in basal conditions may cause significant gradients in h that also have important glaciological consequences. For example, near ice stream shear margins N increases abruptly [e.g., *Kamb*, 2001; *Raymond*, 1996; *Schoof*, 2004] to locations where substantial freezing is expected to occur beneath ice ridges, whereas N is likely low enough within the fast-flowing stream interiors that $h = 0$ and equation (12) is satisfied. Abrupt spatial and temporal transitions in h are facilitated by lower fluid supply rates and values of V_{\max} . Treating the fringe temperature gradient as constant, the maximum freezing rate is predicted to occur when V given by equation (18) satisfies

$$V_{\max} \approx \frac{V^* \theta_l^{-\alpha}}{1 - \phi(1 - \theta_l^{-\beta})} \left\{ 1 - \frac{T_m(1 - \phi)(\rho_s - \rho_l)g}{G \rho_i \mathcal{L} \left[1 - \phi(1 - \theta_l^{-\beta}) \right]} \right\}, \quad (27)$$

which is reduced when V^* is smaller.

[55] As first pointed out by *Christoffersen and Tulaczyk* [2003], there are similarities between the layers of debris-free and debris-rich ice that are sometimes seen in basal ice [e.g., *Carsey et al.*, 2002], and the layering that occurs during frost heave. The conditions for mechanical equilibrium described in section 2 can be extended to examine how the effective stress supported by particle contacts p_p varies with depth within the fringe [e.g., *Rempel*, 2007, equation (7)]. In integral form, this is expressed as

$$p_p \approx N - \frac{\rho_i \mathcal{L}}{T_m} \left(\phi S_i (T_m - T) - \int_{T_f}^T \phi S_i dT \right) + \frac{\rho_i^2 V \eta}{\rho_l^2} \int_{l-h}^z \frac{(1 - \phi S_i)^2}{k} dz - (1 - \phi)(\rho_s - \rho_l)g(z - l + h),$$

where the second term on the right accounts for the load borne by pore ice that extends beneath z to temperatures warmer than T , the third term accounts for the change in fluid pressure required by Darcy's law to supply freezing at rate V , and the final term accounts for the reduction in overburden with height that accompanies the reduced sediment loading. In a differential form that is amenable to being solved at the same time as equation (24) for the scaled temperature profile, this implies that

$$\frac{\partial p_p}{\partial z} \approx -\phi p_f \beta (1 - S_i) \frac{\partial \theta}{\partial z} + \frac{\rho_i^2 V \eta}{\rho_l^2} \frac{(1 - \phi S_i)^2}{k} - (1 - \phi)(\rho_s - \rho_l)g, \quad (28)$$

where $p_p = N$ at $z = l - h$. When h exceeds the level where $V = V_{\max}$, p_p can reach a minimum within the interior of the fringe, and when h is sufficiently thick that $p_p = 0$ at this minimum the entrained till particles separate and an ice lens forms. For the steady state calculations shown in Figure 5 and the case where $N = 20$ kPa, a lens first forms 2 m below the glacier base once $h \approx 6$ m. At higher effective stress h must get thicker still before the ice-till interactions within the fringe are sufficiently strong to cause particle separation. A lens forms once $h \approx 10.5$ m when $N = 40$ kPa, for example. Though often much larger, at a minimum the thicknesses of debris-rich and debris-free bands that are formed in this way are expected to scale with the distance over which the temperature changes by $T_m - T_f$ and so alters S_i and k . Because of the shallow temperature gradients that are typically encountered beneath glaciers, this suggests banding on scales that are too large to explain the millimeter- to centimeter-scale layering that is sometimes observed.

[56] The analysis presented here is applied toward simplified model systems that intentionally ignore several physical interactions that are known to be important in many glacial settings. Pore compressibility, or poroelasticity, is an important consideration in modeling subglacial hydrology and it is believed to play a particularly important roll in governing the behavior of ice streams [e.g., *Clarke*, 1987; *Fowler*, 2003; *Kamb*, 2001; *Tulaczyk et al.*, 2000]. In the current treatment ϕ is assumed constant, but large changes in p_p can occur within the fringe and these may cause postentrainment particle rearrangements. Indeed,

Christoffersen et al. [2006] report particle concentrations in the basal ice layer of Kamb Ice Stream that are lower than expected from random closed packing in the unfrozen till beneath. *Christoffersen et al.* [2006] developed a model that includes poroelastic effects in the unfrozen till and produces centimeter-scale layering patterns that are similar to those they observe. *Rempel et al.* [2007] pointed out that the lensing condition in that model is quite different from those used in established frost heave treatments, which rely on connected ice in a fringe to support overburden and relieve the stresses on particle contacts, but appears instead to be equivalent to a “piping condition” wherein the fluid pressure balances the overburden. *Christoffersen et al.* [2007] dispute this interpretation, but emphasize that the additional physical effects represented in their model are required to obtain predictions of fine-scale layering. The effects of poroelasticity throughout the frozen and unfrozen till, together with other physical interactions, such as those that result from the presence of solutes, certainly merit further exploration (for a recent review of subglacial processes, see *Clarke* [2005]). Lensing need not occur only through the mechanism of stress transfer proposed by *O’Neill and Miller* [1985] that is behind the formulation used here. For example, *Peppin et al.* [2006, 2007] observed ice lenses form during solidification in colloidal suspensions as a result of a morphological instability related to poroelastic effects.

[57] As illustrated by the modeling exercises of section 3, the conditions of thermodynamic and mechanical equilibrium across the till-glacier interface ultimately produce a boundary condition between the thermomechanical ice-flow problem above and the subglacial hydrological problem beneath. The long-term average rate of heat flow through the basal ice and the large-scale average effective stress at the bed can be estimated from the heat and force balance on and within the glacier, whereas the short-term and small-scale variations in the distribution of effective stress are more closely associated with the mechanics of subglacial drainage [e.g., *Engelhardt and Kamb*, 1997; *Kamb*, 2001; *Flowers and Clarke*, 2002; *Hindmarsh*, 1997; *Walder and Fowler*, 1994]. The variations in N that are produced by flow between subglacial channels were examined by *Iverson* [2000] to predict profiles of regelation layer thickness. Similar extensions can be made to the current model in order to predict spatial variations in h and examine potential erosion patterns, while including the effects of lateral gradients in system properties and driving parameters. Further progress will ultimately require models that couple treatments of glacier flow and subglacial hydrology in a self-consistent fashion.

5. Conclusions

[58] The physical interactions that govern freezing in porous media are well known from studies of ground-freezing in subaerial environments. Though the overburden beneath glaciers is much larger, the effective stress N is often within the typical range that is considered by models for frost-heaving behavior in fine-grained sediments. A fringe of partially frozen sediment is predicted to extend beneath the glacier base when $N > p_f$. Significant glacial

sediment transport can be produced by sliding at the fringe base. With the low temperature gradients that are characteristic of the basal environment, the fringe thickness h is expected to often reach decimeters to meters in scale. Equation (19) gives approximate bounds on the steady state h when the effects of fluid flow through the fringe can be neglected. The temperature-dependent ice saturation S_i and permeability k are key sediment properties that determine quantitative aspects of the freezing behavior. More fine-grained sediments are characterized by larger p_f so that fringe formation begins at higher N . Fine-grained sediments also typically have low k , so that the maximum rate that meltwater can be transported through the fringe is modest. For a glacier that is perched above a given sediment, larger h is predicted with higher N and the lower heat input that accompanies slower rates of sliding W_s . Changes in N or W_s are expected to cause transient behavior, with the freezing rate V adjusting rapidly to satisfy force-balance constraints, and h relaxing on the timescale for conduction of latent heat.

Appendix A: Approximate δp for $h = 0$

[59] When there is no fringe, the effective stress and freezing or melting rate can be related to the basal temperature. In such cases the change in fluid pressure δp through the premelted films overlying the uppermost soil particles can be an important component of the force balance on the glacier base [e.g., *Worster and Wettlaufer*, 1999]. Lubrication theory and mass balance considerations lead to [*Rempel and Worster*, 1999]

$$\delta p \approx \int_0^{\theta_c} \sin \theta \cos \theta \left[\int_{\theta_c}^{\theta} \frac{6\eta R^2}{d^3} V \sin \phi \, d\phi \right] d\theta,$$

where d is the thickness of the premelted films and θ_c is the angle from the vertical at which the separation of the soil particles and ice surface becomes much greater than d . Treating d as approximately constant I find that

$$\delta p \approx \frac{\eta R^2 V}{d^3} f(\theta_c),$$

where $f(\theta_c) = 4(1 - \cos^3 \theta_c) - 3 \cos \theta_c (1 - \cos 2\theta_c)$. It is useful to express the particle size R in terms of the pressure scale p_f , which can be related to the curvature of the pore throats R_p . Assuming that $R = R_p/\alpha_p$ for some $\alpha_p < 1$, I find that $R = 2\gamma_{il}/(\alpha_p p_f)$, where γ_{il} is the surface energy of the ice-liquid interface. Using this result, for the case where interfacial premelting is controlled by van der Waals interactions, I find that

$$d^{-3} \approx \lambda^{-3} \left(\frac{T_m - T_l}{T_m} + \frac{\alpha_p p_f}{\rho_i \mathcal{L}} \right),$$

where T_l is the basal temperature and λ is a length scale that measures the range of the van der Waals interactions. Geometrical arguments suggest that the approximate cut-off

angle satisfies $\sin\theta_c \approx (1 + \alpha_p)/(1 + \alpha_p/\theta_l)$, where $\theta_l = (T_m - T_l)/(T_m - T_f) \leq 1$. Putting this together, I find that

$$\delta p \approx \frac{4\eta\gamma_{il}^2 V}{\lambda^3 \alpha_p p_f \rho_i \mathcal{L}} \left(1 + \frac{\theta_l}{\alpha_p}\right) f(\theta_c). \quad (\text{A1})$$

Appendix B: Conservation of Mass and Energy

[60] Considering the change in water mass (both liquid and ice) within an arbitrary volume due to mass flux across its surface, reveals that

$$\frac{\partial}{\partial t} \int_{\Omega} [\phi S_i \rho_i + \phi(1 - S_i) \rho_l] d\Omega = - \int_{\Gamma} \rho_l \mathbf{V} \cdot d\Gamma,$$

where Γ is a surface element with unit outward normal of the volume Ω , and \mathbf{V} is the rate of ice motion. Using the divergence theorem on the right and recognizing that the volume is arbitrary gives

$$\nabla \cdot \mathbf{V} = \frac{\rho_l - \rho_i}{\rho_i} \frac{\partial(\phi S_i)}{\partial t} - \frac{\rho_l}{\rho_i} \frac{\partial\phi}{\partial t}, \quad (\text{B1})$$

where the water and ice themselves are both treated as incompressible. When changes in the porosity within the fringe can be neglected, the divergence of ice velocity is proportional to the 10% density difference between liquid water and ice. The flow can be regarded as approximately solenoidal (i.e., $\nabla \cdot \mathbf{V} \approx 0$) for many applications and I assume \mathbf{V} to be spatially uniform in the model calculations.

[61] In cases where poroelastic effects are appreciable and $\partial\phi/\partial t$ cannot be neglected, the principal of mass conservation applied to the particle matrix requires that $\nabla \cdot \mathbf{V}_p = \partial\phi/\partial t$ where \mathbf{V}_p is the average flux of particles across the total cross-sectional area. Though \mathbf{V}_p is assumed negligible in the model calculations, it is convenient to include it in deriving the equation that describes the temperature evolution.

[62] The conservation of energy within the fringe can be expressed in terms of specific enthalpies h_k of the sediment particles (subscript s), ice (subscript i), and liquid water (subscript l), so that

$$\begin{aligned} & \frac{\partial}{\partial t} \int_{\Omega} [(1 - \phi) \rho_s h_s + \phi S_i \rho_i h_i + \phi(1 - S_i) \rho_l h_l] d\Omega \\ &= \int_{\Gamma} \{ -[\phi S_i \rho_i + (1 - \phi S_i) \rho_l h_l] \mathbf{V} - \rho_s h_s \mathbf{V}_s + K_e \nabla T \} \cdot d\Gamma, \end{aligned} \quad (\text{B2})$$

where the effective thermal conductivity is K_e . Changes in enthalpy are related to changes in temperature by $dh_k = c_k dT$, where c_k is the specific heat at constant pressure of the k th component. The latent heat of fusion is $h_l - h_i \equiv \mathcal{L}$. With these relations and the mass conservation condition from equation (B1), the energy conservation condition reduces to

$$\begin{aligned} \bar{\rho} c_e \frac{\partial T}{\partial t} - [\rho_l + (\rho_l - \rho_i) \phi S_i] \mathcal{L} \frac{\partial(\phi S_i)}{\partial t} + \rho_l \phi S_i \mathcal{L} \frac{\partial\phi}{\partial t} \\ = -[\rho_i c_i \phi S_i + (1 - \phi S_i) \rho_i c_l] \mathbf{V} \cdot \nabla T - \rho_s c_s \mathbf{V}_s \cdot \nabla T \\ - \rho_l \mathcal{L} \mathbf{V} \cdot \nabla(\phi S_i) + \nabla \cdot (K_e \nabla T). \end{aligned}$$

where $\bar{\rho} c_e \equiv (1 - \phi) \rho_s c_s + \phi S_i \rho_i c_i + \phi(1 - S_i) \rho_l c_l$ is the heat capacity of the partially frozen till.

[63] The heat conservation condition simplifies considerably when the ice saturation is only a function of temperature and when porosity variations can be neglected. The sediment particles are assumed fixed so $\mathbf{V}_p = 0$ in this case. I introduce the Stefan number $\mathcal{S} \equiv \rho_i \mathcal{L} / [\bar{\rho} c_e (T_m - T_f)]$ as a measure of the relative importance of latent heat to sensible heat, and rewrite equation (B2) for the case where ϕ is constant as

$$\begin{aligned} & \left[1 - \phi \mathcal{S} \left(1 + \phi S_i \frac{\rho_l - \rho_i}{\rho_i} \right) (T_m - T_f) \frac{dS_i}{dT} \right] \frac{\partial T}{\partial t} \\ & \approx - \left[1 + (1 - \phi) \frac{\rho_l c_l - \rho_s c_s}{\bar{\rho} c_e} - \phi \mathcal{S} (T_m - T_f) \frac{dS_i}{dT} \right] \mathbf{V} \cdot \nabla T \\ & + \frac{1}{\bar{\rho} c_e} \nabla \cdot (K_e \nabla T). \end{aligned} \quad (\text{B3})$$

If the ice saturation is assumed to follow the empirical relation given by equation (5) this can be written as

$$\begin{aligned} & \left[1 + \phi \beta \mathcal{S} \left(1 + \phi S_i \frac{\rho_l - \rho_i}{\rho_i} \right) \left(\frac{T_m - T_f}{T_m - T} \right)^{\beta+1} \right] \frac{\partial T}{\partial t} \\ & \approx - \left[1 + (1 - \phi) \frac{\rho_l c_l - \rho_s c_s}{\bar{\rho} c_e} + \phi \beta \mathcal{S} \left(\frac{T_m - T_f}{T_m - T} \right)^{\beta+1} \right] \mathbf{V} \cdot \nabla T \\ & + \frac{1}{\bar{\rho} c_e} \nabla \cdot (K_e \nabla T). \end{aligned}$$

Figure 3 suggests that the temperature at the farthest extent of pore ice differs from the bulk melting temperature by considerably less than 1°C for most porous media, and β has an average value of 0.4. Since $\rho_l \mathcal{L} \approx 3 \times 10^8 \text{ J/m}^3$ and $\bar{\rho} c_e = O(10^6) \text{ J/(m}^3\text{C)}$, $\mathcal{S} \approx 10^{2\circ\text{C}}/(T_m - T_f)$ and $\phi \beta \mathcal{S}$ is expected to greatly exceed unity. The density difference between ice and water is only 10% and the difference in volumetric heat capacity between liquid water and the sediment particles is not expected to be large in comparison to $\bar{\rho} c_e$. Accordingly, I approximate the energy conservation condition through the fringe as

$$- \left[\phi \rho_i \mathcal{L} \frac{dS_i}{dT} \right] \left(\frac{\partial T}{\partial t} + \mathbf{V} \cdot \nabla T \right) \approx \nabla \cdot (K_e \nabla T), \quad (\text{B4})$$

where only vertical gradients and transport are considered in the modeling that follows. Equation (B4) describes how conduction dissipates the latent heat that accompanies changes to the ice saturation caused by changes in temperature and ice motion through a temperature gradient.

[64] The thermal conductivity of the ice-liquid-particle mixture changes as freezing progresses. *Andersland and Ladanyi* [2004] suggest that K_e can be approximated using a geometric mean so that

$$K_e \approx K_p^{(1-\phi)} K_i^{S_i \phi} K_l^{(1-S_i)\phi}, \quad (\text{B5})$$

where $K_i \approx 2.2 \text{ W/(m}^\circ\text{C)}$, $K_l \approx 0.57 \text{ W/(m}^\circ\text{C)}$, and K_p are the thermal conductivities of the ice, liquid, and particles. The thermal conductivities of common mineral particles vary considerably, with randomly oriented quartz grains toward the high end at $K_p \approx 8.4 \text{ W/(m}^\circ\text{C)}$ (though some

sulfides and oxides have conductivities that are several times higher), and values for framework silicates typically around $K_p \approx 2 \text{ W/(m}^\circ\text{C)}$ [Clauser and Huenges, 1995]. I adopt an intermediate value of $K_p = 4 \text{ W/(m}^\circ\text{C)}$ in the model calculations here so that the effective thermal conductivity of the unfrozen sediments is $K_e(S_i = 0) = K_u \approx 2 \text{ W/(m}^\circ\text{C)}$ for $\phi = 0.35$. Equation (B4) can be written as

$$-\left[\phi\rho_i\mathcal{L}\frac{dS_i}{dT}\right]\left(\frac{\partial T}{\partial t} + \mathbf{v} \cdot \nabla T\right) \approx K_e\nabla^2 T + \phi K_e \ln\left(\frac{K_i}{K_l}\right) \frac{dS_i}{dT} |\nabla T|^2, \quad (\text{B6})$$

where the second term on the right can be neglected when

$$\frac{K_e|\nabla T|}{\rho_i\mathcal{L}|V|} \ln\left(\frac{K_i}{K_l}\right) \ll 1.$$

For a conductive flux through the fringe of $K_e|\nabla T| \approx 0.1 \text{ W/m}^2$, gradients in thermal conductivity produce effects that are negligible in comparison to those of latent heat release when $|V| \gg 14 \text{ mm/a}$. For slower rates of melting or freezing, as are typical of the calculations presented here, the nonlinear term in equation (B6) is important.

Appendix C: Numerical Scheme for Transient Calculations

[65] To facilitate numerical solutions, it is useful to write scaled equations in terms of the dimensionless undercooling $\theta \equiv (T_m - T)/(T_m - T_f)$ and the diffusive timescale $\tau \equiv \kappa_i t/l^2$, where $\kappa_i = K_i/\rho_i c_i$ is the thermal diffusivity of ice. Moreover, I define the stretched coordinates $x \equiv (z - l + h)/(l - h)$, and $y \equiv (z - l)/h$ to fix the location of the moving fringe boundary. Substituting into equation (5) for $S_i(T)$ and defining the Stefan number as $\mathcal{S} \equiv \rho_i \mathcal{L}/[\rho_c c_e(T_m - T_f)]$, the transformed equations (22)–(25) become

$$\begin{aligned} \frac{\partial \theta}{\partial \tau} &= -\frac{x+1}{l-h} \frac{dh}{d\tau} \frac{\partial \theta}{\partial x} + \left(\frac{l}{l-h}\right)^2 \frac{\kappa_u}{\kappa_i} \frac{\partial^2 \theta}{\partial x^2}, \quad -1 \leq x \leq 0 \\ \frac{\partial \theta}{\partial \tau} &= \frac{y}{h} \frac{dh}{d\tau} \frac{\partial \theta}{\partial y} + \left(\frac{l}{h}\right)^2 \frac{\kappa_e \theta^{\beta+1}}{\kappa_i \phi \beta \mathcal{S}} \frac{\partial^2 \theta}{\partial y^2} - \frac{Vl^2}{h\kappa_i} \frac{\partial \theta}{\partial y} \left[1 - \frac{\kappa_e}{hSV} \ln\left(\frac{K_i}{K_l}\right) \frac{\partial \theta}{\partial y}\right], \\ &\quad -1 \leq y \leq 0 \\ \frac{\partial \theta}{\partial \tau} &= l^2 \frac{\partial^2 \theta}{\partial z^2}, \quad l \leq z \leq 2l, \\ \frac{dh}{d\tau} &= \frac{l^2}{\kappa_i} \\ &\cdot \left\{ \frac{K_u(T_m - T_f)}{\phi \beta \rho_i \mathcal{L} h} \frac{\partial^2 \theta}{\partial y^2} - \left[V - \frac{K_u(T_m - T_f)}{\rho_i \mathcal{L} h} \ln\left(\frac{K_i}{K_l}\right) \frac{\partial \theta}{\partial y} \right] \frac{\partial \theta}{\partial y} \right\}_{y=-1} \\ &\times \left[\frac{h}{l-h} \frac{\partial \theta}{\partial x} \Big|_{x=0} + \frac{Q_f h}{K_u(T_m - T_f)} \right]^{-1}. \end{aligned}$$

where $\kappa_e = K_e/\rho_c c_e$ is the effective thermal diffusivity in the partially frozen fringe and $\kappa_u = \kappa_e(S_i = 0)$ is the diffusivity in the unfrozen sediments.

[66] The boundary conditions are formulated as follows. As suggested by the schematic diagram in Figure 1b, I impose a constant geothermal heat flux at $z = 0$ so that

$$\frac{K_u}{l-h} \frac{\partial \theta}{\partial x} \Big|_{x=-1} = \frac{Q_g}{T_m - T_f}.$$

The temperature at the fringe base is set to T_f so that

$$\theta(x = 0, \tau) = \theta(y = -1, \tau) = 1.$$

Frictional work increases the heat flux at the fringe base so that

$$\frac{K_e}{h} \frac{\partial \theta}{\partial y} \Big|_{y=-1} - \frac{K_u}{l-h} \frac{\partial \theta}{\partial x} \Big|_{x=0} = \frac{Q_f}{T_m - T_f},$$

where $Q_f = \mu N W_s$. Continuity of temperature at the top of the fringe requires that

$$\theta(z = l^+, \tau) = \theta(y = 0, \tau).$$

The change in phase of the residual liquid at the top of the fringe causes a jump in the heat flux so that

$$K_i \frac{\partial \theta}{\partial z} \Big|_{z=l^+} - \frac{K_e}{h} \frac{\partial \theta}{\partial y} \Big|_{y=0} = V \rho_c c_e \mathcal{S} [1 - \phi(1 - \theta_l^{-\beta})].$$

The temperature gradient a distance l above the glacier base is set to

$$\frac{\partial \theta}{\partial z} \Big|_{z=2l} = \frac{Q_g + Q_{f0}}{K_i(T_m - T_f)} + \frac{V_0 S K_e}{\kappa_e K_i},$$

where $Q_{f0} = \mu N_0 W_s$, and V_0 and N_0 represent the initial steady state freezing rate and effective stress. The final condition required to close the system comes from the mechanical constraint given by equation (16). This is transformed to obtain the freezing rate at the fringe base as

$$\begin{aligned} V \approx & \left(\frac{\rho_l}{\rho_i}\right)^2 \frac{p_f}{\eta h \int_{-1}^0 (1 - \phi S_i)^2 / k \, dy} \\ & \cdot \left[\theta_l + \phi \int_{\theta_l}^1 S_i \, d\theta - \frac{N}{p_f} + \frac{(\rho_s - \rho_l) g h (1 - \phi)}{p_f} \right], \end{aligned}$$

where the pressure scale $p_f \equiv \rho_i \mathcal{L}(T_m - T_f)/T_m$ is used once again (see equation (18)).

[68] The solution procedure involved writing evolution equations accurate to second order in space for the temperature at each node and the rate of change in fringe thickness. The initial temperature field and freezing rate were set to steady state values calculated using the procedure discussed in section 3.2 for the given initial h_0 and N_0 . The effective stress was then changed and the system was solved using the MATLAB stiff ODE solvers. Five hundred nodes were placed within the fringe itself for the calculations shown

here and l was chosen as $\sqrt{2\kappa_i t_{\max}}$ when the calculations extended to $t = t_{\max}$.

Notation

c_i	ice heat capacity at constant pressure.	α	exponent in permeability description.
c_l	liquid heat capacity at constant pressure.	α_p	ratio of pore throat radius to particle radius.
c_p	particle heat capacity at constant pressure.	β	exponent in ice-saturation description.
d	premelted film thickness.	γ_{il}	ice-liquid interfacial energy.
g	acceleration of gravity.	η	liquid viscosity.
G	temperature gradient.	λ	characteristic range of van der Waals forces.
h	fringe thickness.	μ	friction coefficient.
h_i	specific enthalpy of ice.	$\Pi(d)$	ice-substrate intermolecular force per unit area.
h_l	specific enthalpy of liquid.	ϕ	till porosity.
h_p	specific enthalpy of particles.	σ_n	normal stress.
H	glacier thickness.	ρ_i	ice density.
k	ice-saturation-dependent permeability.	ρ_l	liquid density.
k_0	permeability of water-saturated till.	ρ_s	till particle density.
\mathcal{K}	curvature of ice-liquid interface.	$\bar{\rho}c_u$	volumetric heat capacity of unfrozen till.
K_e	effective thermal conductivity in fringe.	Ψ	function to account for nonlinearities in $T(z)$.
K_i	thermal conductivity of ice.	θ	dimensionless undercooling.
K_l	thermal conductivity of liquid.	θ_l	dimensionless undercooling at $z = l$.
K_p	thermal conductivity of particles.	κ_e	effective thermal diffusivity in fringe.
K_u	effective thermal conductivity of unfrozen till.	κ_i	thermal diffusivity of ice.
l	location of glacier-till interface.	κ_u	effective thermal diffusivity of unfrozen till.
\mathcal{L}	latent heat of fusion.		
N	effective stress.		
N_0	initial effective stress.		
p	pressure in pores immediately beneath ice.		
p_f	thermomolecular force per unit area at temperature T_f .		
\bar{p}_f	average fluid pressure at ice base.		
p_i	ice pressure.		
p_l	liquid pressure.		
p_m	reference pressure.		
p_p	stress supported by particle contacts.		
p_T	thermomolecular force per unit area.		
p_n	nonhydrostatic fluid force per unit area.		
p_0	overburden force per unit area.		
δp	difference between pore pressure and average fluid pressure.		
Q_b	basal heat flux.		
Q_f	dissipative heat flux.		
Q_g	geothermal heat flux.		
R	characteristic particle size.		
R_p	characteristic radius of pore throats.		
S	Stefan number.		
S_i	ice saturation level.		
\bar{S}_i	average ice saturation level in fringe.		
SSA	specific surface area.		
t	time.		
T	temperature.		
T_f	temperature at which ice enters pore space.		
\bar{T}_l	temperature at glacier-till interface.		
T_m	bulk melting temperature at reference pressure.		
U	Darcy transport rate.		
V	freezing rate.		
V_0	initial freezing rate.		
V^*	velocity scale.		
V_{\max}	maximum steady state freezing rate.		
W_s	glacier sliding rate.		
z	vertical coordinate.		

[69] **Acknowledgments.** This work benefitted from numerous discussions with the visitors, fellows, and faculty of the 2006 summer school in Geophysical Fluid Dynamics at WHOI, and from a productive visit to BAS in spring 2007. I am particularly grateful for insights shared by Andrew Fowler, Richard Hindmarsh, Christian Schoof, John Wettlaufer, and Grae Worster, and to Neal Iverson for providing me with a preprint. Funding was provided by NSF OPP0440841.

References

- Alley, R. B., and D. R. MacAyeal (1994), Ice-rafted debris associated with binge/purge oscillations of the Laurentide Ice Sheet, *Paleoceanography*, *9*, 503–511.
- Alley, R. B., K. M. Cuffey, E. B. Evenson, J. C. Strasser, D. E. Lawson, and G. J. Larson (1997), How glaciers entrain and transport basal sediment: Physical constraints, *Quat. Sci. Rev.*, *16*, 1017–1038.
- Alley, R. B., D. E. Lawson, E. B. Evenson, J. C. Strasser, and G. J. Larson (1998), Glaciohydraulic supercooling: A freeze-on mechanism to create stratified, debris-rich basal ice: II. Theory, *J. Glaciol.*, *44*, 563–569.
- Andersland, O. B., and B. Ladanyi (2004), *An Introduction to Frozen Ground Engineering*, 363 pp., Chapman and Hall, New York.
- Broecker, W. S. (1994), Massive iceberg discharges as triggers for global climate change, *Nature*, *372*, 431–434.
- Cahn, J. W., J. G. Dash, and H.-Y. Fu (1992), Theory of ice premelting in monosized powders, *J. Cryst. Growth*, *123*, 101–108.
- Carsey, F., A. Behar, A. L. Lane, V. Realmuto, and H. Engelhardt (2002), A borehole camera system for imaging the deep interior of ice sheets, *J. Glaciol.*, *48*, 622–628.
- Christoffersen, P., and S. Tulaczyk (2003), Response of subglacial sediments to basal freeze-on: 1. Theory and comparison to observations beneath the West Antarctic Ice Sheet, *J. Geophys. Res.*, *108*(B4), 2222, doi:10.1029/2002JB001935.
- Christoffersen, P., S. Tulaczyk, F. D. Carsey, and A. E. Behar (2006), A quantitative framework for interpretation of basal ice facies formed by ice accretion over subglacial sediment, *J. Geophys. Res.*, *111*, F01017, doi:10.1029/2005JF000363.
- Christoffersen, P., S. Tulaczyk, F. D. Carsey, and A. Behar (2007), Reply to comment by Rempel et al. on “A quantitative framework for interpretation of basal ice facies formed by ice accretion over subglacial sediment,” *J. Geophys. Res.*, *112*, F02037, doi:10.1029/2006JF000732.
- Clarke, G. K. C. (1987), Subglacial till: A physical framework for its properties and processes, *J. Geophys. Res.*, *92*(B9), 9023–9036.
- Clarke, G. K. C. (2005), Subglacial processes, *Annu. Rev. Earth Planet. Sci.*, *33*, 247–276.
- Clauser, C., and E. Huenges (1995), Thermal conductivity of rocks and minerals, in *Rock Physics and Phase Relations, A Handbook of Physical Constants*, *AGU Ref. Shelf*, vol. 3, edited by T. J. Ahrens, pp. 105–126, AGU, Washington, D. C.
- Dash, J. G. (1989), Thermomolecular pressure in surface melting—Motivation for frost heave, *Science*, *246*(4937), 1591–1593.
- Dash, J. G., A. W. Rempel, and J. S. Wettlaufer (2006), The physics of premelted ice and its geophysical consequences, *Rev. Mod. Phys.*, *78*, 695–741.

- Engelhardt, H., and B. Kamb (1997), Basal hydraulic system of a West Antarctic ice stream: Constraints from borehole observations, *J. Glaciol.*, *44*, 223–230.
- Fitzsimons, S. J., K. J. McManus, P. Sirota, and R. D. Lorrain (2001), Direct shear tests of materials from a cold glacier: Implications for landform development, *Quat. Int.*, *86*, 129–137.
- Flowers, G. E., and G. K. C. Clarke (2002), A multicomponent coupled model of glacier hydrology: 1. Theory and synthetic examples, *J. Geophys. Res.*, *107*(B11), 2287, doi:10.1029/2001JB001122.
- Fowler, A. C. (2003), On the rheology of till, *Ann. Glaciol.*, *37*, 55–59.
- Fowler, A. C., and W. B. Krantz (1994), A generalized secondary frost heave model, *SIAM J. Appl. Math.*, *54*, 1650–1675.
- Gilpin, R. R. (1980), Wire regelation at low temperatures, *J. Colloid Interface Sci.*, *77*, 435–438.
- Hallet, B., L. Hunter, and J. Bogen (1996), Rates of erosion and sediment evacuation by glaciers: a review of field data and their implications, *Global Planet. Change*, *12*, 213–235.
- Hindmarsh, R. (1997), Deforming beds: Viscous and plastic scales of deformation, *Quat. Sci. Rev.*, *16*, 1039–1056.
- Hulbe, C. L., D. R. MacAyeal, G. H. Denton, J. Kleman, and T. V. Lowell (2004), Catastrophic ice shelf breakup as the source of Heinrich event icebergs, *Paleoceanography*, *19*, PA1004, doi:10.1029/2003PA000890.
- Iverson, N. R. (1993), Regelation of ice through debris at glacier beds—Implications for sediment transport, *Geology*, *21*, 559–562.
- Iverson, N. R. (2000), Sediment entrainment by a soft-bedded glacier: A model based on regelation into the bed, *Earth Surf. Processes Landforms*, *25*, 881–893.
- Iverson, N. R., and R. M. Iverson (2000), Distributed shear of subglacial till due to Coulomb slip, *J. Glaciol.*, *47*, 481–488.
- Iverson, N. R., and D. J. Semmens (1995), Intrusion of ice into porous-media by regelation: A mechanism of sediment entrainment by glaciers, *J. Geophys. Res.*, *100*, 10,219–10,230.
- Iverson, N. R., R. W. Baker, and T. S. Hooyer (1998), Ring-shear studies of till deformation: Coulomb-plastic behavior and distributed strain in glacier beds, *J. Glaciol.*, *44*, 634–642.
- Iverson, N. R., T. S. Hooyer, U. H. Fischer, D. Cohen, P. L. Moore, M. Jackson, G. Lappégard, and J. Kohler (2007), Soft-bed experiment beneath Engabreen, Norway: Regelation infiltration, basal slip, and bed deformation, *J. Glaciol.*, *53*, 323–340.
- Jacka, T. H., S. Donoghue, J. Li, W. F. Budd, and R. M. Anderson (2003), Laboratory studies of the flow rates of debris-laden ice, *Ann. Glaciol.*, *37*, 108–112.
- Kamb, B. (2001), Basal zone of the west Antarctic ice streams and its role in lubrication of their rapid motion, in *The West Antarctic Ice Sheet: Behavior and Environment*, *Antarct. Res. Ser.*, vol. 77, edited by R. B. Alley and R. A. Bindschadler, pp. 157–199, AGU, Washington, D. C.
- Kavanaugh, J. L., and G. K. C. Clarke (2006), Discrimination of the flow law for subglacial sediment using in situ measurements and an interpretation model, *J. Geophys. Res.*, *111*, F01002, doi:10.1029/2005JF000346.
- Knight, P. G. (1997), The basal ice layer of glaciers and ice sheets, *Quat. Sci. Rev.*, *16*, 975–993.
- Larson, G. J., D. E. Lawson, E. B. Evenson, R. B. Alley, O. Knudson, M. S. Lachniet, and S. L. Goetz (2006), Glaciohydraulic supercooling in former ice sheets?, *Geomorphology*, *75*, 20–32.
- Lawson, W. (1996), The relative strengths of debris-laden basal ice and clean glacier ice: Some evidence from Taylor Glacier, Antarctica, *Ann. Glaciol.*, *23*, 270–276.
- Nixon, J. F. (1991), Discrete ice lens theory for frost heave in soils, *Can. Geotech. J.*, *28*, 843–859.
- O'Neill, K., and R. D. Miller (1985), Exploration of a rigid ice model of frost heave, *Water Resour. Res.*, *21*(3), 281–296.
- Paterson, W. S. B. (1994), *The Physics of Glaciers*, 480 pp., Pergamon, London.
- Peppin, S. S. L., J. A. W. Elliott, and M. G. Worster (2006), Solidification of colloidal suspensions, *J. Fluid Mech.*, *554*, 147–166.
- Peppin, S. S. L., M. G. Worster, and J. S. Wettlaufer (2007), Morphological instability in freezing colloidal suspensions, *Proc. R. Soc., Ser. A*, *463*, 723–733.
- Philip, J. R. (1980), Thermal fields during regelation, *Cold Reg. Sci. Technol.*, *3*, 193–203.
- Raymond, C. (1996), Shear margins in glaciers and ice sheets, *J. Glaciol.*, *42*, 90–102.
- Rempel, A. W. (2007), The formation of ice lenses and frost heave, *J. Geophys. Res.*, *112*, F02S21, doi:10.1029/2006JF000525.
- Rempel, A. W., and M. G. Worster (1999), The interaction between a particle and an advancing solidification front, *J. Cryst. Growth*, *205*(3), 427–440.
- Rempel, A. W., J. S. Wettlaufer, and M. G. Worster (2001), Interfacial premelting and the thermomolecular force: Thermodynamic buoyancy, *Phys. Rev. Lett.*, *87*, 088501.
- Rempel, A. W., J. S. Wettlaufer, and M. G. Worster (2004), Premelting dynamics in a continuum model of frost heave, *J. Fluid Mech.*, *498*, 227–244.
- Rempel, A. W., J. S. Wettlaufer, and M. G. Worster (2007), Comment on “A quantitative framework for interpretation of basal ice facies formed by ice accretion over subglacial sediments” by Poul Christoffersen et al., *J. Geophys. Res.*, *112*, F02036, doi:10.1029/2006JF000701.
- Roberts, M. J., F. S. Tweed, A. J. Russell, O. Knudsen, D. E. Lawson, G. J. Larson, E. B. Evenson, and H. Björnsson (2002), Glaciohydraulic supercooling in Iceland, *Geology*, *30*, 439–442.
- Schoof, C. (2004), On the mechanics of ice-stream shear margins, *J. Glaciol.*, *50*, 208–218.
- Shreve, R. L. (1984), Glacier sliding at subfreezing temperatures, *J. Glaciol.*, *30*, 341–347.
- Telford, J. W., and J. S. Turner (1963), The motion of a wire through ice, *Philos. Mag.*, *8*, 527–531.
- Tulaczyk, S., B. Kamb, and H. Engelhardt (2000), Basal mechanics of Ice Stream B. I. Till mechanics, *J. Geophys. Res.*, *105*, 463–481.
- Walder, J. S., and A. Fowler (1994), Channelized subglacial drainage over a deformable bed, *J. Glaciol.*, *40*, 3–15.
- Worster, M. G., and J. S. Wettlaufer (1999), The fluid mechanics of premelted liquid films, in *Fluid Dynamics at Interfaces*, edited by W. Shyy and R. Narayanan, pp. 339–351, Cambridge Univ. Press, Cambridge, U. K.

A. W. Rempel, Department of Geological Sciences, University of Oregon, Eugene, OR 97403-1272, USA. (rempe@uoregon.edu)